Summer 2012

Evaluation of Autonomous Robotic Milling Methodology for Natural Tooth-Shaped Implants Based on SKO Optimization

Yongki Yoon
Old Dominion University

EVALUATION OF AUTONOMOUS ROBOTIC MILLING METHODOLOGY FOR NATURAL TOOTH-SHAPED IMPLANTS BASED ON SKO OPTIMIZATION

by

Yongki Yoon
B.S. February 1999, Inha University, South Korea
M.S. August 2008, Old Dominion University

A Dissertation Submitted to the Faculty of
Old Dominion University in Partial Fulfillment of the
Requirements for the Degree of

DOCTOR OF PHILOSOPHY

MECHANICAL AND AEROSPACE ENGINEERING

OLD DOMINION UNIVERSITY
August 2012

Approved by:

Jen-Kuang Huang (Director)

Frederic D. McKenzie (Member)

Gene Hou (Member)

Stacie I. Ringleb (Member)

ABSTRACT

EVALUATION OF AUTONOMOUS ROBOTIC MILLING METHODOLOGY FOR NATURAL TOOTH-SHAPED IMPLANTS BASED ON SKO OPTIMIZATION

Yongki Yoon
Old Dominion University, 2012
Director: Dr. Jen-Kuang Huang

Robotic surgery is one of the most demanding and challenging applications in the field of automatic control. One of the conventional surgeries, the dental implantation, is the standard methodology to place the artificial tooth root composed of titanium material into the upper or lower jawbone. During the dental implant surgery, mechanical removal of the bone material is the most critical procedure because it may affect the patient's safety including damage to the mandibular canal nerve and/or piercing the maxillary sinus. With this problem, even though short term survival rates are greater than 95%, long term success rate of the surgery is as low as 41.9% in 5 years. Since criteria of bone loss should be less than 0.2 mm per year, a high degree of anatomical accuracy is required. Considering the above issues leads to the employment of more precise surgery using computer assisted medical robots.

In this dissertation, a computer-aided open-loop intra-operative robotic system with pre-operative planning is presented to improve the success rate of the dental implantation using different types of milling algorithms that also incorporate natural root-shaped implants.

This dissertation also presents the refinement and optimization of three-dimensional (3D) dental implants with the complex root shapes of natural teeth. These root shapes are too complex to be drilled manually like current commercial implants and

are designed to be conducive to robotic drilling utilizing milling algorithms. Due to the existence of sharp curvatures and undercuts, anatomically correct models must be refined for 3D robotic milling, and these refined shapes must be shown to be optimized for load bearing. Refinement of the anatomically correct natural tooth-shaped models for robotic milling was accomplished using Computer-Aided-Design (CAD) tools for smoothing the sharp curvatures and undercuts. The load bearing optimization algorithm is based on the Soft-Kill Option (SKO) method, and the geometries are represented using non-uniform rational B-spline (NURBS) curves and surfaces. Based on these methods, we present optimized single and double root-shaped dental implants for use with robotic site preparation.

Evaluation of phantom experiment has led us to investigate how the position, orientation, and depth of the robotic drilling defined with the dental tool exhibit accuracy and efficiency.

To My Parents: Byung-Lee Yoon and Kilhwa Kim

ACKNOWLEDGMENTS

I would like to gratefully thank my advisor Dr. Jen-Kuang Huang for his guidance, understanding, encouragement and endless support of this dissertation. He always has inspired me to think deeply about the subjects not only as a scientist but also as a philosopher.

I wish to express my deepest gratitude to Dr. Frederic D. McKenzie for giving me the opportunity to work on an excellent project. Also, many thanks go out to my committee members, Dr. Gene Hou and Stacie I. Ringleb for their research guidance.

I thank my colleague Xiaoyan Sun for her efforts and invaluable discussions of this research. Her effort and suggestions have made a difference. I also extend my gratitude to my friend Adam Przekop for his suggestion regarding finite element analysis.

Very special thanks go out to my parents and brother whose love, support and understanding in so many different ways has enabled this undertaking to actually proceed.

TABLE OF CONTENTS

LIST OF TABLES

LIST OF FIGURES

Figure Page

CHAPTER 1

INTRODUCTION

1.1 Problem Description

Robotic surgery is one of the most demanding and challenging applications in the field of automatic control. One of the conventional surgeries, dental implantation, is the standard technology to place artificial tooth root composed of titanium material into the upper or lower jawbone. During dental implant surgery, mechanical removal of bone material is the most critical procedure because it may affect the patient's safety by damaging the mandibular canal nerve and/or piercing the maxillary sinus. Even though short term survival rates are greater than 95%, long term success rate of the surgery is as low as 41.9% in 5 years. Since criteria of bone loss should be less than 0.2 mm per year, a high degree of anatomical accuracy is required [1].

Considering the above issues leads to the employment of a more precise surgical method using computer assisted medical robots. The importance of robotic surgery in medical engineering and the need for superior design techniques and tools for such systems is underscored. One objective of this dissertation is to develop a computerized robotic system capable of performing different types of milling algorithms to incorporate natural root-shaped implants with an open-loop. This new framework offers a significant potential for precise milling processes when compared to the conventional approach. The tool provides an interface allowing design modifications to be made with rapid assessment of the resulting effects. One can explore various milling options efficiently, and the graphical nature of the technique can suggest necessary modifications to achieve the desired open-loop traits. A second objective of this dissertation is utilization of the

new tool for operation of robotic surgery. The tool is used to operate the robotic system that goes beyond baseline control architectures typically generated with open-loop design strategies.

1.2 Literature Review

Recent advancements in medical robotics have entered the operating room, bringing countless opportunities for new developments and improvements. Surgical operations are now assisted by intelligent systems in many aspects such as preoperative planning, image guidance, tele-operated surgical robots, surgical assistants and augmented devices [2, 3].

1.2.1 Surgical Robot

Kwoh et al in 1985 introduced the first surgical robot for computerized tomography (CT) guided brain surgery [4]. An autonomous robotic system called prostate-ctomy robot (PROBOT) was then created to aid in the transurethral resection of the prostate [5]. However, due to the large envelop of the industrial robot motion, patient safety was the most critical issue during the surgical operation. Since then, research has been focused on the concept of the special-purpose mechanism which can be controlled by constraints. In 1992, the ROBODOC, a modified selective compliant assembly robot arm (SCARA) manipulator, was used in orthopedic surgery to mill out the implant cavity in the femur for total hip replacement [6]. ROBODOC was the first medical robot approved by the Food and Drug Administration (FDA). However, the automated endoscopic system for optimal positioning (AESOP) used for minimally invasive surgery was the first commercially available robot approved by the FDA in 1994 [7, 8]. In the late

1990s, the complete robotic systems called Zeus (Computer Motion, Goleta, CA, USA) and da Vinci (Intuitive Surgical, Mountain View, CA, USA) were introduced for laparoscopic and minimally invasive surgery [9].

1.2.2 Dental Implants and the Finite Element Method in Dentistry

Dental implants have been widely used to aid replacement of tooth loss in the mandible or maxilla. A variety of materials, including single-crystal sapphire, stainless steel, and titanium, are used for designing implants. Orthopedic surgeons experimented with titanium to check biocompatibility in 1940, while corrosion tests were performed in the 1950s. In 1969, Brånemark first introduced the osseointegration of the implant with the bone structure and the possibility of the clinical use in intraosseous implantation [10, 11].

For the last several decades, research was conducted for enhancing bone apposition to titanium surfaces. Experimental and numerical results demonstrate that bone adapts to mechanical stimuli [12-16]. The natural root shape may improve the survival rate based on our understanding of implant failures. Compared to a dental implant, a natural tooth has a periodontal ligament, located between the tooth and the bone, for mechanical stress absorption. Therefore, this research was focused on developing the optimized implant shape which is able to attenuate the biological threat for a long-term success rate. However, this process was not easy to perform via clinical trials due to the considerable radiation dosage from CT examination for the patient over the healing period [17].

Bony structural remodeling using computational methods has been a popular methodology over the past three decades. In this manner, finite element analysis (FEA)

has been practically applied to the bio-structural objects for determining global stress and displacement [18, 19].

In 1982, Cook et al. developed a mechanical bony model which was incorporated into a 3D FEA of porous rooted dental implants. The mechanical test was also performed to compare to the FEA result of which implant with tissue ingrowth-bonded interface showed a better stress distribution [20]. One year later, Skalak investigated the relationship of stress distribution and load transfer in osseointegrated prosthesis [21]. Since then, a number of papers for different types of dental implants were published regarding the implant shapes, loading conditions, material types, and boundary conditions [22-27]. Recently, the research related to dental implants has been focused on the biocompatible implant design and shape optimization with respect to biological growth [28-33].

1.3 Contributions of the Research

A new extension of robotic surgery using a fully integrated autonomous image-guided robotic system is one contribution of this research. This new design extension can be applied simply to a variety of medical areas including dental implantation. This new framework is of major importance because it offers a mechanism to achieve the performance benefits of a highly integrated system designed with a conventional approach, with all the associated advantages thereof. A software tool implementing the control panel is another contribution of the research. The tool operates and displays the various commands and allows multiple operating options to control the robot efficiently. A final contribution of the research is development of natural root-shaped implants using topology optimization. A fully integrated surgical robotic system is achieved beyond that

attainable from standard design practice.

1.4 Dissertation Outline

The layout of this dissertation is given below. Chapter 2 presents the background of surgical robotics. Highlights of the more commonly known robotic systems are summarized, and system characteristics and a simple example are provided. In Chapter 3, general robotic systems and the proposed system are reviewed. In Chapter 4 the framework for the drilling procedure of the robotic system is presented including basic equations. The reader is taken through the sequential transformation steps of robot motion. The flow of the program is documented and illustrations are provided. The experiment is performed to investigate how the vibration of the dental tool affects the entire drilling process. The constraints for robot workspace are also employed to describe patient safety issues. Chapter 5 provides an overview of the fully integrated robotic milling system including hardware and software. Chapter 6 describes the optimized natural root-shaped implants. The chapter explains the 2D and 3D finite element models for dental implants and capabilities for use in dentistry. Chapter 7 utilizes this result to explore the potential of the Phantom experiment with a fully integrated robotic system. As a benchmark, this chapter also considers the robotic milling sequences for natural tooth-shaped implants. Lastly, general conclusions are given in Chapter 8.

CHAPTER 2

BACKGROUND OVERVIEW

2.1 Introductory Remarks

The main purpose of this chapter is to introduce and summarize the autonomous dental implantation using a robot arm. Because this application is in the early stages of development, it is not as practical to apply in implantation in comparison to general robotic surgery. An autonomous dental implantation technique will be introduced based on robotic operation. To provide the proper context, and because of similarities, other applications of robotic surgery are also reviewed here.

2.2 Background of Robotic Surgery

Within the extensive research field of robotics, surgical robotics is an interdisciplinary area in clinical applications. Over the past decades, robotic systems have been developed rapidly and made it possible for robotic surgery in orthopaedics, neurosurgery, laparoscopic procedures, ophthalmic surgery, and cardiac surgery. Table 2.1 summarizes the comparison between a human surgeon and robotic operation. The table shows that one of the main advantages of a robot is the geometric accuracy and repeatability during the surgical operation, while a human surgeon has more flexibility to integrate the multiple information and make decisions.

Davies categorized the integrated surgical system as three phases [34]: (a) pre-operative planning, (b) intra-operative intervention, and (c) post-operative assessment. Knee arthroscopy, one of the minimally invasive surgeries, is a good example to describe the surgical procedures. First in pre-operative planning, a surgeon resects the cartilage with small incisions in the tissue with the help of the computed tomography (CT) and

magnetic resonance imaging (MRI) for anatomical information. Thus, a surgeon can make a decision whether the robot will impinge on the patient or not. In the intra-operative stage, it is necessary to match the data precisely from the pre-operative site with the patient's anatomy. Thus, registration is the most important step in the robotic system. It is a well-known approach to place the markers or fiducials on the anatomical structure for obtaining their location. Finally, the post-operative phase can observe the quality of the procedure. Figure 2.1 shows the commercially available robotic system upon the above manner.

Table 2.1 Advantage and Disadvantage between Human and Robot [35]

Robots	• Good geometric accuracy and repeatability • Stable and untiring • Can be designed for a wide range of scales • Resistant to radiation and infection • Diverse sensors in control	• Poor judgment • Limited dexterity and hand-eye coordination • Expensive • Difficult to construct and debug

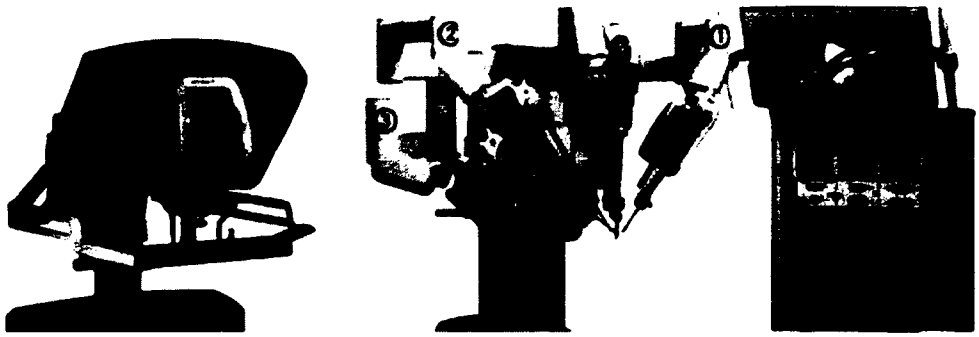

Figure 2.1 Overall System of da Vinci Robotic System including Console, surgical robot, and vision system (Intuitive Surgical, Inc.)

Compared to other robotic surgeries, there is less research going on regarding dental implantation. Most of the dental robots are haptic-based and use a computer-assisted approach for the implantation [36-39]. Thus, as seen in Figure 2.2, we proposed the fully integrated image-guided robotic system for automated dental implantation using the above procedure [40]. Patient specific 3D models are accomplished from Cone-beam CT in the preoperative process, and implantation planning is performed with these virtual models. In order to transform the preoperative plan to intro-operative operation a patient registration is conducted with the robot and coordinate measurement system (CMM).

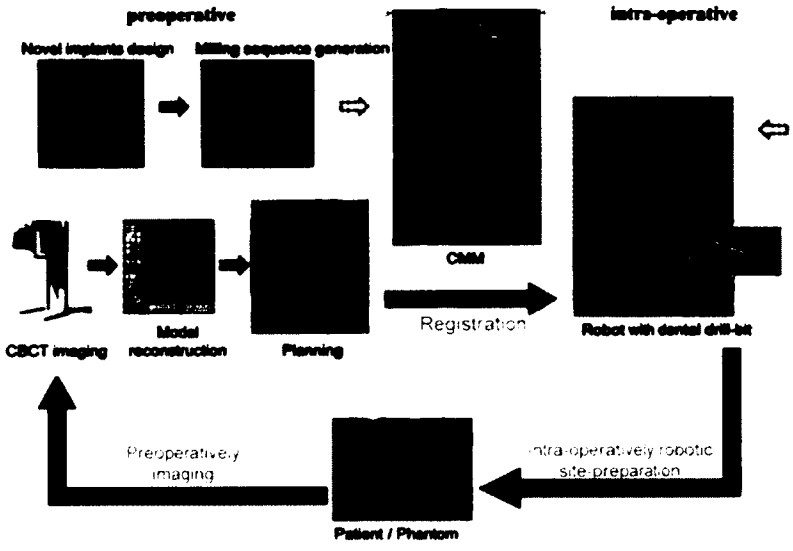

Figure 2.2 System Overview for the Autonomous Robotic Dental Implantation [41]

2.3 Finite Element for Dental Implant

Advancements of computing schemes for biological analysis and computer-aided design (CAD) have led to rapid development in biomechanical applications ranging from biotechnology to tissue engineering [42]. Based on the designed CAD geometrical configuration, finite element analysis (FEA) in dental research has been significantly used for several decades to reduce time and cost [20, 43-47] and to provide specific quantitative information at any location within a geometrical model. Thus, FEA has become a highly required analytical tool for assessment in dentistry. This research utilized a combination of CAD analysis and FEA optimization to design natural root shapes including a two-root shape for dental implants that is intended for automated robotic site preparation [40] and subsequent manual implantation. These novel shapes are intended to provide a significant increase in the stability of implants which we believe will increase the long term (> 5 years) success rate of dental implants.

Modeling the exact geometry of the commercial implant including the thread helix of the screw and the screw bore is essential for finite element analysis [48]. In this dissertation, however, two types of natural root-shape implants were created based on the press-fit type of implant which would not be screwed into the bone but may support many different types of surface treatments and shapes that could contribute to enhanced stability. Thus, sophisticated 3D models are required to better understand the mechanical behavior of the jaw bone structure and prosthetic dental restorations [49]. Fok et al. (2006) [50] provide a direct comparison of experimental and theoretical results in biomechanical studies to achieve congruencies for validation. A simplified mandibular segment with implants was modeled using MD Patran 2010 which we have utilized. The first step of modeling is to use CAD to define the desired bone and implant geometry. Then this is followed by defining the material behavior in terms of the Young's modulus and Poisson's ratio for various mandibular bone components and the implant for FEA. After applying the load and boundary conditions, the various parameters and their contributions to the stress profile can be evaluated.

Based on our FEA results, a biologically-inspired adaptive growth method was introduced to design the optimized implant shapes which are able to reduce the stress distribution around the interface between the bones and the implant [50]. Topology optimization of mechanical components requires computationally demanding methods and several methods have been proposed. In order to address dental implant design, one of the methodologies, Soft-Kill Option optimization related to biologically adaptive growth, has been adapted to bone remodeling and implant optimization [50, 51]. With this method, the topology of the body and associated implant is completely defined and

various parts of the body may have non-uniform local stresses based upon the impact of the implant. The objective of the optimization process is to find the best structural layout of an implant to minimize the maximum local stress [52].

2.4 System Safety

In the surgical robotic system, safety is one of the major concerns when considering system hardware or software failure. In order to improve system safety in the aspect of hardware, kinematic redundancy and sensors are commonly used in a surgical robot. Although this methodology has efficiency to detect and recover the system failure consistently, redundancy also increases hardware and software complexity, which makes the robotic system more costly [53-55]. Another common approach to improve safety in robotic surgery is to provide motion constraints of the predefined robot workspace. Davies, et al. described four possible programming modes for the range of motion [56]: free mode, position mode, trajectory mode, and region mode. Thus, the patient can avoid potential unintended damage to areas outside the point of operation. One more important concern in surgical robotic system safety is sterilization and infection control in the operating room. This is usually achieved by covering the entire surgical robot, with the exception of the surgical end-effector, with sterile drapes.

CHAPTER 3

ROBOTIC APPLICATION IN DENTAL IMPLANTATION

3.1 Robot Overview

The Mitsubishi RV-3S Robot shown in Figure 3.1 is a joint arm robot type with six degrees of freedom classified as anthropomorphic articulated robots. Each joint has one freedom of rotation around its own axis. The robot has a reach of 642 mm and speeds of up to 5,500 mm/s with a repeatability of ± 0.02 mm. Table 3.1 summarizes the operational range of the RV-3S robot. Joints 1 and 6 provide a rotational angular motion around the z-axis in the xy plane. Joints 2, 3 and 5 revolute around the y-axis, while joint 4 revolutes around the x-axis.

Figure 3.1 Fully Integrated Mitsubishi RV-3S Robot Manipulator

Table 3.1 Operation Range of Joint for Mitsubishi RV-3S Robot

Ability	Joint	Range
Operation Range	J1	340° (±170°)
	J2	225° (-90° to +135°)
	J3	191° (-20° to +171°)
	J4	320° (-160° to +160°)
	J5	240° (±120°)
	J6	720° (±360°)

The Mitsubish Electric Factory Automation (MELFA) BASIC IV was chosen as a default robot programming language for implementation. The robot was integrated with a CR1-571 controller unit, and a teach pendant, and was connected to the personal computer using RS232 communication cable.

3.2 System Accuracy

Accuracy makes a robot position its end-effector at a predefined location in 3D space. Also, it is a function of the precision of the robot arm kinematic model, tool, and fixture models. Thus, manipulator accuracy is important to match the robot geometry to the robot solution in use by precisely measuring and calibrating link lengths, joint angles, and mounting positions [57]. In this section, calibration of the dental tool attachment and registration procedure were considered.

3.2.1 Calibration

The transformation between the robot end-effector and the robot tool tip is defined by their frames. This transformation remains constant during the whole operational process and can be calibrated when the tool is mounted on the robot. When a tool is mounted to the robot tool plate, the points where the actions must happen can be different due to the geometry of the tool. In order to obtain the precise pose after attaching the tool, a calibration process is required.

As illustrated in Figure 3.2, the position of a rigid body in space is expressed in terms of the position of a suitable point on the body with respect to a reference frame, while its orientation is expressed in terms of the components of the unit vectors of a frame attached to the body [58].

Consider an arbitrary point $\boldsymbol{P}$ in space. Let p_2 be the vector of coordinates of $\boldsymbol{P}$ with respect to the reference frame O_0. Let p_1 and R_1^0 be the vector and rotational matrix describing the origin of frame O_1 with respect to frame O_0. Let also r_{12} be the vector of coordinates of $\boldsymbol{P}$ with respect to frame O_1. Thus, the position, $\boldsymbol{P}$, can be expressed as

$$p_2 = p_1 + R_1^0 r_{12} \cdot \tag{3.1}$$

Since Equation (3.1) represents the coordinate transformation between two frames, one can also calculate the r_{12} using inverse transformation (see Equation (3.2)).

$$r_{12} = -R_0^1 p_1 + R_0^1 p_2 \tag{3.2}$$

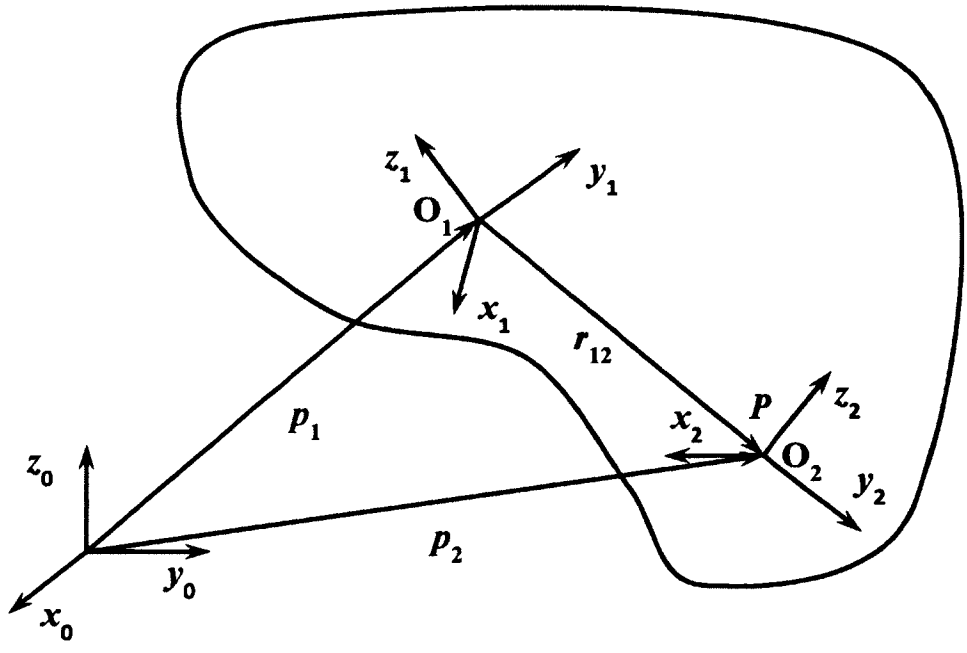

Figure 3.2 Representation of a Point P in Different Coordinate Frames

Considering the above equations, Figure 3.3 illustrates the operation coordinate system (OCS) of the robot arm. The frame of a target position in OCS is the relative position of the tip of the drill-bit with respect to robot origin frame, denoted as P_{tip}. Since the dental drill-bit is attached to the end-effector rigidly, the relative position, $v_{cal} = [x, y, z, \phi, \theta, \psi]$, is constant with respect to the robot end-effector frame. Meanwhile, the rotation and position information of the end-effector in the robot coordinate system (i.e. the OCS) is known from the robot controller software, which can be recorded as R_{rob} and t_{rob}, respectively. R_{rob} and t_{rob} together transfer a coordinate in the robot end-effector frame to the coordinate in robot OCS.

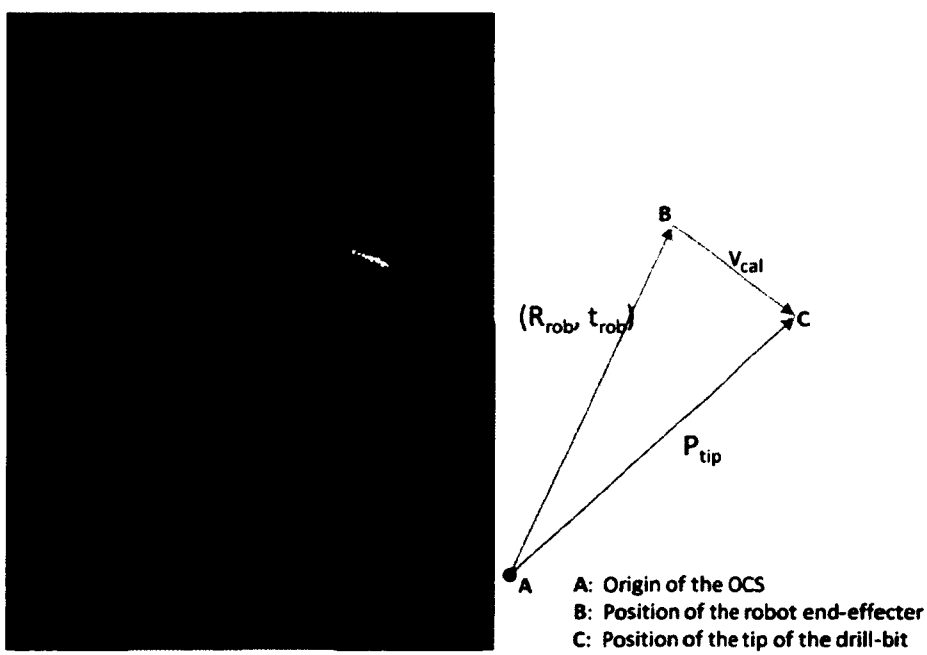

Figure 3.3 Illustration of Calibration in the OCS [57]

Using Equation (3.1), one can re-express the tool tip position as

$$[P_{tip}] = [t_{rob}]_i + [R_{rob}]_i[v_{cal}] \tag{3.3}$$

where $i = 1, 2, \ldots n$.

Note index i indicates the amount of pose variation of the robot. The tool transformation for the dental drill-bit top can be computed by manually positioning the tip to a fixed pivot point with different orientations (see Figure 3.4). Thus, the relative position v_{cal} can be determined by applying a standard pivot calibration based on Equation (3.2). However, it only sets up a one direction mapping from (R_{rob}, t_{rob}) to P_{tip}. For the dental tool frame in Figure 3.5, orientation is also an important factor which needs to be considered for the surgical operation due to angle offset between the end-effector and alignment of the drill-bit. Thus, angles of the xy-plane, yz-plane and xz-plane were also calibrated. A checkerboard with a standard line distance of 1 cm was applied to determine the rotation matrix between the tool frame and the end-effector of the robot. As seen in the figure, the robot end-effector was aligned with the line on the checkerboard, and the relative angles between the dental drill-bit and each plane in the Cartesian coordinate system of the robot were computed using the teaching pendant. Considering these procedures, offset pose from the robot end-effector to dental drill-bit tip was calculated as v_{cal} = [191.50, -0.14, 40.51, 0, 17.5, 0].

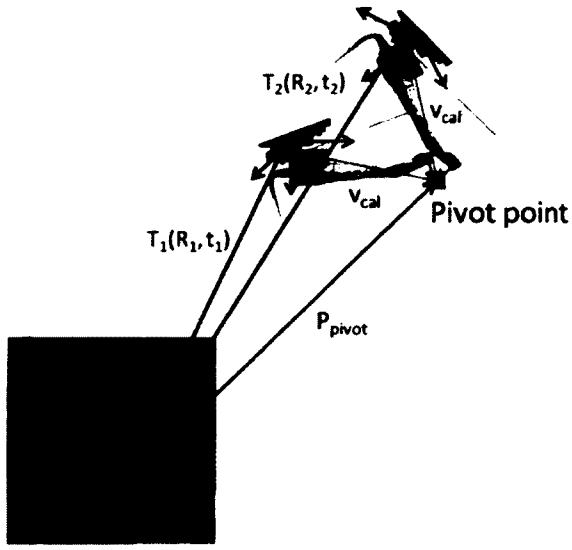

Figure 3.4 Pivot Calibration for the Robot Tool Frame [57]

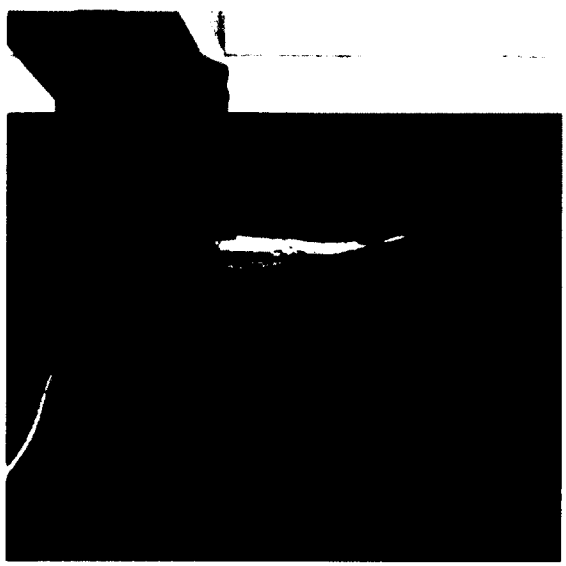

Figure 3.5 Orientation Calibration for the Tool Frame [57]

3.2.1 Registration

As already mentioned in the previous section, it is necessary to define a reference for each object involved in the registration, in a particular tool, anatomical object and the

robot. These frames have to be aligned during the rigid registration step at the beginning of the surgical intervention. Three coordinate systems were considered in the dental implantation system[40]: the virtual coordinate system (VCS), the reference coordinate system (RCV), and the operation coordinate system(OCS). In Figure 3.6, the registration process will transfer the preoperative surgical plan in VCS to the intra-operative robotic operation in OCS with the coordinate measurement system (CMM) in RCV.

X. Sun, et al. described in greater detail the whole procedure and the experiment results using the two-step registration method[41]. Five fiducials and eight fixed registration points in Figure 3.7 were used for registration in VCS and RCS and in RCS and OCS, respectively. Table 3.2 shows significant improvement in the registration accuracy. Final target registration error (TRE) is 0.36 ± 0.13 mm, which is comparable with similar systems[59, 60], and the orientation error in the OCS after registration is 1.99 ± 1.27° as shown in Table 3.3.

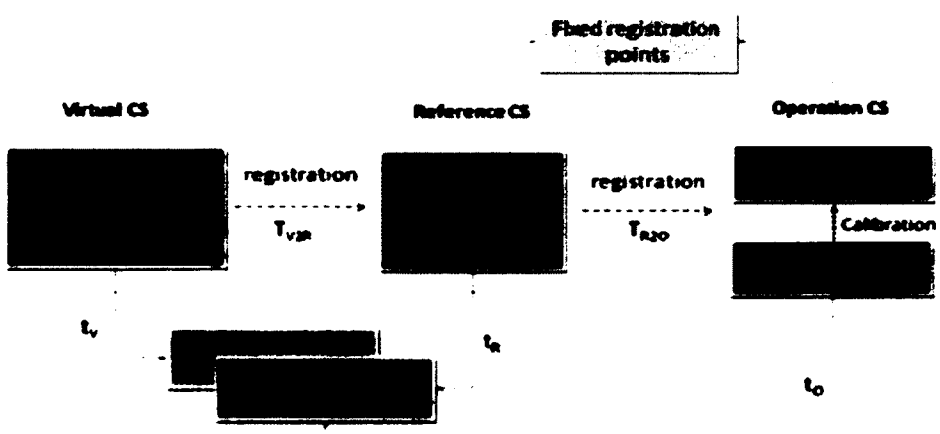

Figure 3.6 The Relationship Among Coordinate Systems [40]

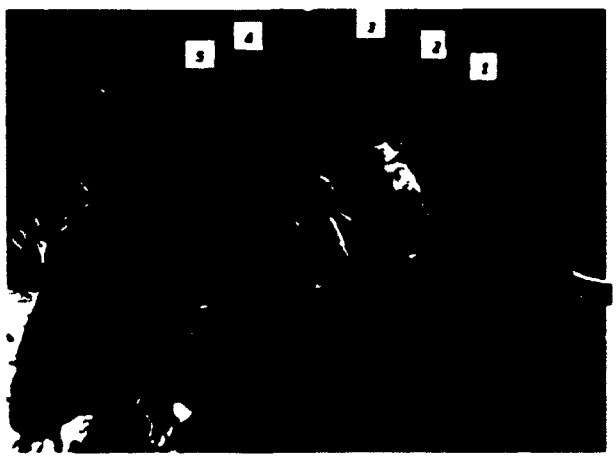

Figure 3.7 Configuration of Five Fiducials and Eight Fixed Registration Points [40]

Table 3.2 Registration Results for Positioning Accuracy in [mm] Unit [61]

	before Faro fixation				after Faro fixation				after Faro fixation and CS orientation pre-alignment			
	step 1		step 2		step 1		step 2		step 1		step 2	
Target #	FRE	TRE	FRE	TRE	FRE	TRE	FRE	TRE	FRE	TRE	FRE	TRE
1	0.23	1.82	0.18	2.29	0.20	1.90	0.19	1.74	0.10	0.43	0.19	0.44
2	0.29	0.80	6	0.89	0.27	0.86	4	1.15	0.15	0.23	4	0.41
3	0.42	0.16		0.74	0.43	0.26		0.42	0.15	0.23		0.50
4	0.28	0.80		1.18	0.33	0.71		0.64	0.18	0.07		0.17
5	0.23	1.80		2.03	0.26	1.72		1.76	0.16	0.25		0.30
MEAN	0.29	1.08	/	1.42	0.30	1.09	/	1.14	0.15	0.24	/	0.36
SD	0.08	0.71	/	0.70	0.08	0.69	/	0.61	0.03	0.13	/	0.13

Table 3.3 Measured Orientation Error After Registration [61]

planned angle	15°		30°		45°	
Target #	actual angle	error	actual angle	error	actual angle	error
1	18.0	3.00	30.3	0.30	42.1	2.90
2	18.6	3.60	29.6	0.40	44.0	1.00
3	17.0	2.00	/	/	42.8	2.20
4	18.6	3.60	29.2	0.80	40.9	4.10
5	16.1	1.10	29.0	1.00	43.1	1.90
MEAN =	17.66	2.66	29.53	0.63	42.58	2.42
SD =	1.09	1.09	0.57	0.33	1.16	1.16

3.3 System Constraints for Dental Implantation

In order to insure penetration of the drill through the bone structure, a dentist has to perform the drilling process by exerting pressure on the drilling tool with acceptable rotary speed and torque of the drill-bit. This may result in a temperature increase caused by the plastic deformation of the chips and friction between the drilling tool and the bone. The problem in bone drilling can sometimes be the occurrence of bone necrosis, which is the irreversible death of bone cells in the vicinity of the hole due to drilling temperature raised over the critical value. Thus, in this section, robotic drilling is employed to make that process stable and accurate.

In order to reduce the drilling temperature, the treatment needs to be performed as quickly as possible so that the heat does not penetrate the bone. This can be achieved by the increase of the drill-bit rotary speed. However, naturally, this speed requires a high pressure force (axial drilling force). The axial penetration force should not be excessive because in some patients it may even cause further fractures. Thus, in our robotic milling system, several constraints were used, such as

- Boundary constraints in tooltip frame (see Figure 3.8);
- Joint constraints (setup no-go area);
- Dental drill-bit speed (heat) and pressure constraints
  rotary speed = 1500 rpm, torque = 20 N-cm.

Once the robot is executed, the dental drill-bit starts to rotate with constrained speed and torque. Figure 3.8 illustrates the boundary constraint for the robot operation. Note that P_s, P_t, and P_{curr} are the start, target, and current position of the robot, respectively. Through the drilling direction, the robot also contains the orientation information such as roll,

pitch, and yaw. Thus, the current position, P_{curr} can be expressed as $P_{curr} = [x, y, z, \phi, \theta, \psi]$.

As seen in the figure, current position will be constrained by cylindrical radius and joint angles. These position and orientation constraints are implemented in the robot controller considering the drill-bit constraints which are independent from the robotic side.

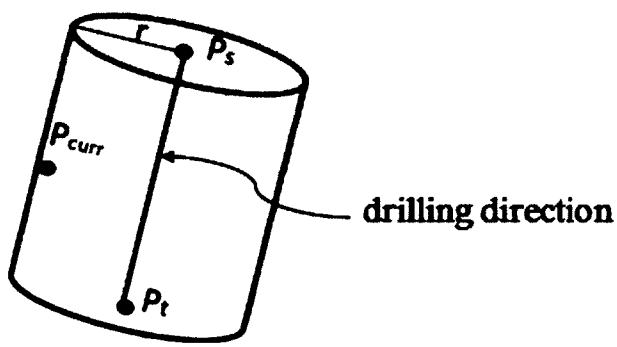

Figure 3.8 Boundary Constraint

CHAPTER 4

ROBOTIC MANIPULATION

A robot manipulator can be described as a kinematic chain of rigid bodies connected by means of revolute or prismatic joints. That means one end of the chain is constrained to a base while an end-effector is fixed to the other end [57]. Therefore, in order to manipulate the robot in space, it is necessary to represent the robot end-effector pose (position and orientation).

4.1 Rotational Transformation

Rotational displacements can be represented in the right-hand rectangular coordinate frame in Figure 4.1. Positive rotations around each axis are counter-clockwise from the origin of the frame O-xyz. In this section, the rotations were made with respect to a fixed frame O-xyz. Figure 4.2, for example, illustrates the coordinate frame O-x′y′z′ obtained by rotating the reference from O-xyz around the x axis for the angle ϕ. Note that axes x and x' are collinear.

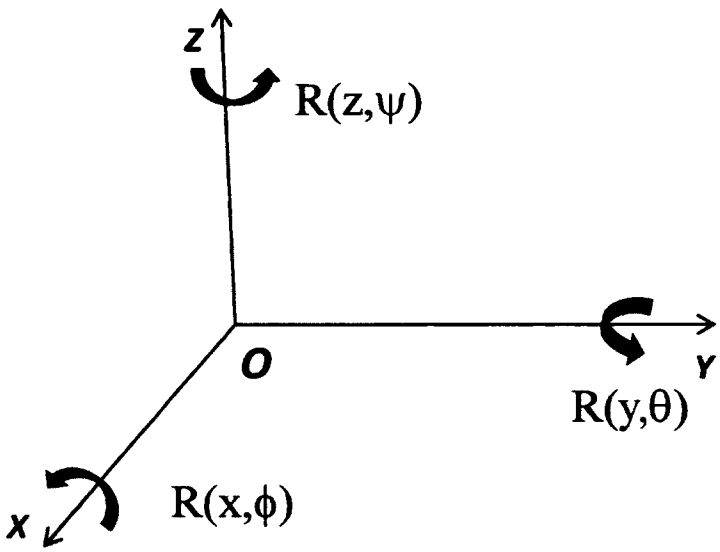

Figure 4.1 Right-Hand Rectangular Frame with Positive Rotations

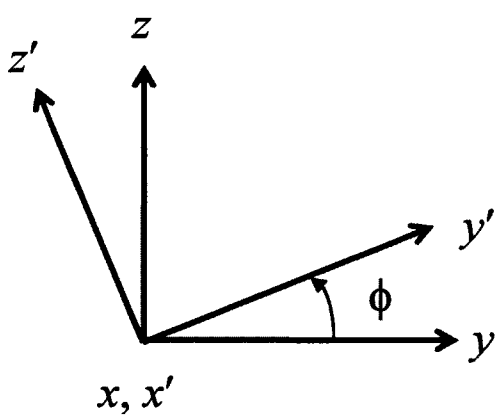

Figure 4.2 Rotation Around x Axis

The elements of 3×3 rotation matrix are cosines of the angles between the axes.

$$R(x,\phi) = \begin{bmatrix} 1 & 0 & 0 \\ 0 & \cos\phi & -\sin\phi \\ 0 & \sin\phi & \cos\phi \end{bmatrix} \tag{4.1}$$

By considering the similarity, one can derive the rotational matrix around the y' axis for the angle θ (see Equation (4.2)).

$$R(y',\theta) = \begin{bmatrix} \cos\theta & 0 & \sin\theta \\ 0 & 1 & 0 \\ \sin\theta & 0 & \cos\theta \end{bmatrix} \tag{4.2}$$

The rotation around the z'' axis is described by the following matrix form.

$$R(z'',\psi) = \begin{bmatrix} \cos\psi & -\sin\psi & 0 \\ \sin\psi & \cos\psi & 0 \\ 0 & 0 & 1 \end{bmatrix} \tag{4.3}$$

4.2 Robot Path Generation

Considering section 4.1, the robot drilling path in Figure 4.3 is generated as follows

$$L = dis(P,T) = \sqrt{d_x^2 + d_y^2 + d_z^2}$$

$$\text{where} \quad \begin{aligned} d_x &= P_x - T_x \\ d_y &= P_y - T_y \\ d_z &= P_z - T_z \end{aligned} \tag{4.4}$$

Let P and T denote the start and target positions with rotational angles by ϕ, θ, ψ with respect to the x, y, and z axes, respectively. Note the robot tool frame described as x_t-y_t-z_t in Figure 4.3. Then final components of the target position will be represented as Equations (4.4) – (4.5).

$$\begin{aligned} T_x &= P_x - L(\sin\phi \sin\psi + \cos\phi \cos\psi \sin\theta) \bullet \text{sign}(T_x - P_x) \\ T_y &= P_y - L(\cos\phi \sin\theta \sin\psi - \sin\phi \cos\psi) \bullet \text{sign}(T_y - P_y) \\ T_z &= P_z - L(\cos\phi \cos\theta) \bullet \text{sign}(T_z - P_z) \end{aligned} \tag{4.5}$$

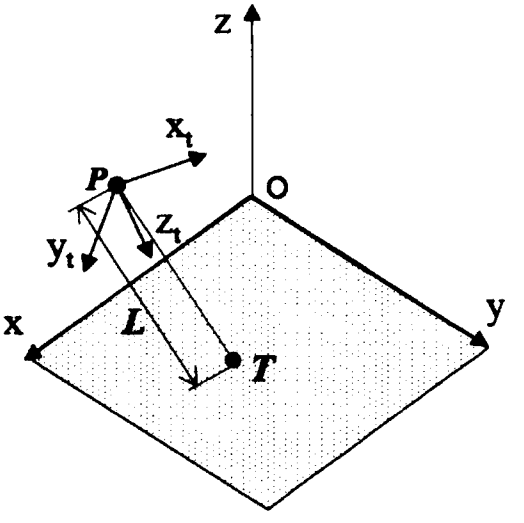

Figure 4.3 Straight Line Drilling Direction from the Start Point to the Target Point

Since a robot arm equipped with a dental tool performs the task by moving its tool tip, the location of the dental drill-bit tip is mainly concerned with respect to the robot's body frame. To describe its trajectory of the geometric volume (cone, cylinder, elliptic cone, and elliptic frustum), the fixed frame was employed for tool tip position.

(1) Cone and Cylinder:

Figure 4.4 illustrates the initial cone volume without any rotation around the axes. To generate the volume, the parametric equation of the cone volume is considered as Equation (4.6) with rotational angle, α, around the z axis at the origin. When z is equal to zero, cylinder shape can be formed.

$$\begin{aligned} x &= r\cos(\alpha) \\ y &= r\sin(\alpha) \\ z &= \left(\frac{h}{r}\right)R \end{aligned} \qquad \text{where } 0 < R < r \text{ and } 0 < \alpha < 2\pi \tag{4.6}$$

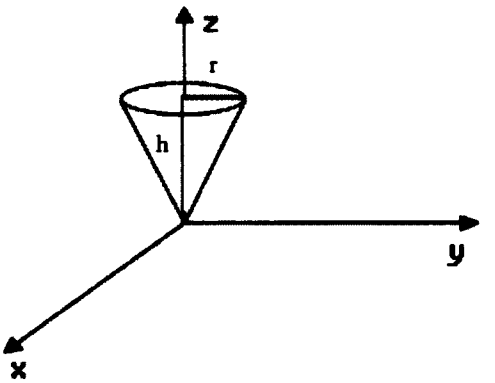

Figure 4.4 Vertical Cone with Equation (4.6)

First, let us consider that volume rotates around the x axis by the angle ϕ, denoted as $R(x, \phi)$ in Equation (4.1). Then one can derive the position components of the tool tip as Equation (4.7).

$$\begin{aligned} x_1 &= x \\ y_1 &= y\cos\phi - z\sin\phi \\ z_1 &= y\sin\phi + z\cos\phi \end{aligned} \tag{4.7}$$

From the current position derived by Equation (4.7), the robot rotates around the y_1 axis by angle θ, denoted as $R(y_1, \theta)$ (see Equation (4.8)).

$$\begin{aligned} x_2 &= x_1\cos\theta + z_1\sin\theta \\ y_2 &= y_1 \\ z_2 &= -x_1\sin\theta + z_1\cos\theta \end{aligned} \tag{4.8}$$

Finally, the robot rotates around the z_2 axis by angle ψ, denoted as $R(z_2, \psi)$.

$$
\begin{aligned}
x_3 &= x_2 \cos\psi - y_2 \sin\psi \\
y_3 &= x_2 \sin\psi + y_2 \cos\psi \\
z_3 &= z_2
\end{aligned}
\tag{4.9}
$$

Thus, one can represent the final conic motion with respect to the current position of the tool tip in Equation (4.10).

$$
\begin{aligned}
x_{new} &= x_{cp} + x_3 \\
y_{new} &= y_{cp} + y_3 \\
z_{new} &= z_{cp} + z_3
\end{aligned}
\tag{4.10}
$$

where cp denotes current position of tool tip.

(2) Elliptic Cylinder:

The following Equations ((4.11) – (4.12)) are for the elliptic cone and elliptic cylinder. In Equation (4.12), angle β is added to get the arbitrary direction of ellipse in the xy-plane (see Figure 4.5). Angle β should be predetermined before the drilling procedure. All other procedures for rotations are the same as the conic form.

$$
e = \sqrt{\frac{a^2 - b^2}{a^2}} \tag{4.11}
$$

where e = eccentricity, a = major axis radius, and b = minor axis radius.

$$
\begin{aligned}
x &= a\cos(\alpha)\cos(\beta) - b\sin(\alpha)\sin(\beta) \\
y &= a\cos(\alpha)\sin(\beta) + b\sin(\alpha)\cos(\beta) \\
z &= 0
\end{aligned}
\tag{4.12}
$$

where $\alpha \in [0, 2\pi)$, and β = the angle between x-axis and major axis.

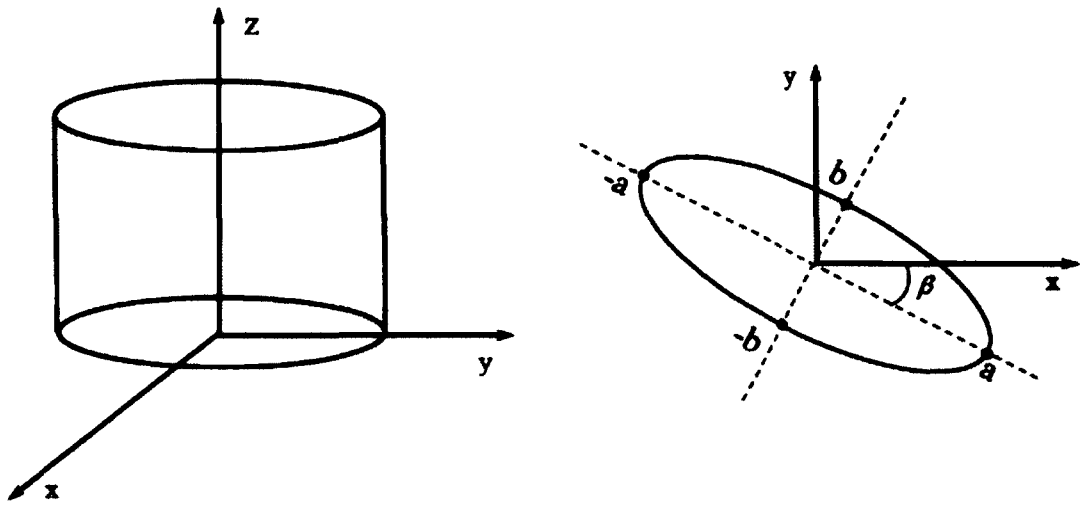

Figure 4.5 Elliptic Cylinder with Equation (4.12)

Thus, the final form can be given as

$$\begin{bmatrix} P \\ \cdots \\ 0 \end{bmatrix} = \begin{bmatrix} R & p \\ \cdots & \cdots \\ 0\,0\,0 & 1 \end{bmatrix} \quad \text{where } p = [x, y, z]^{\mathrm{T}} \text{ and } R = R(z'', \psi)\, R(y', \theta)\, R(x, \phi). \tag{4.13}$$

(3) Elliptic Frustum:

In the same manner, elliptic frustum (see Figure 4.6) is also defined in Equations (4.14) – (4.15) with considering the height increment.

$$\begin{aligned} x &= a\cos(\alpha)\cos(\beta) - b\sin(\alpha)\sin(\beta) \\ y &= a\cos(\alpha)\sin(\beta) + b\sin(\alpha)\cos(\beta) \\ z &= \frac{h}{a}A \end{aligned} \tag{4.14}$$

where $\alpha \in [0, 2\pi)$, β = angle between x-axis and major axis, and $A \in [0, a)$.

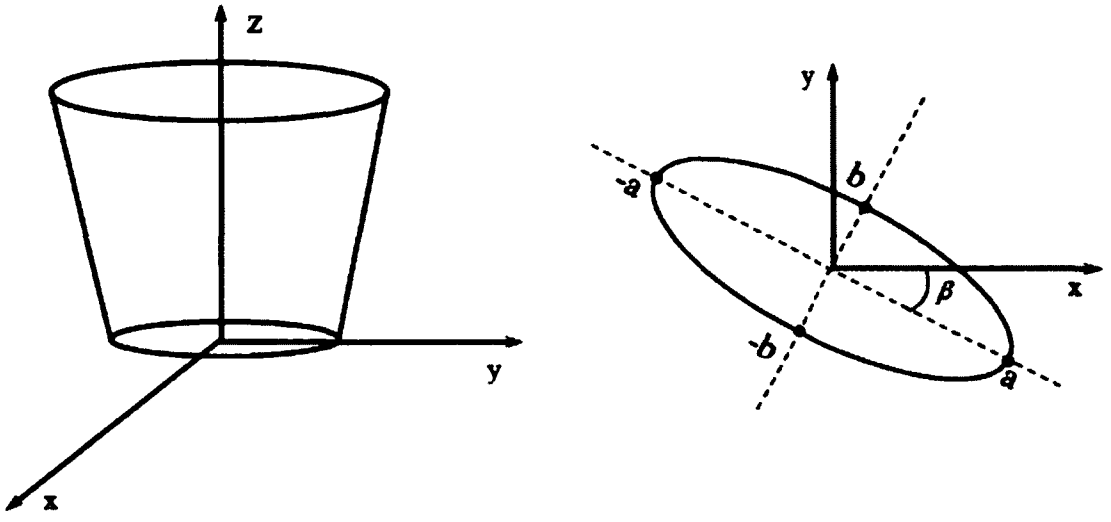

Figure 4.6 Elliptic Frustum with Equation (4.14)

$$\begin{bmatrix} P \\ \cdots \\ 0 \end{bmatrix} = \begin{bmatrix} R & p \\ \cdots & \cdots \\ 0\ 0\ 0 & 1 \end{bmatrix} \quad \text{where } p = [x, y, z]^{\mathrm{T}} \text{ and } R = R(z'', \psi)\, R(y', \theta)\, R(x, \phi) \tag{4.15}$$

Considering the position and orientation of the above robot tool-tip path, Figure 4.7 shows the straight line trajectory of the robot tool tip. Through the straight line the difference between the designed position (red line) and the current position (blue line) of the robot tool tip is less than 0.02 *mm,* which is the robot arm movement resolution.

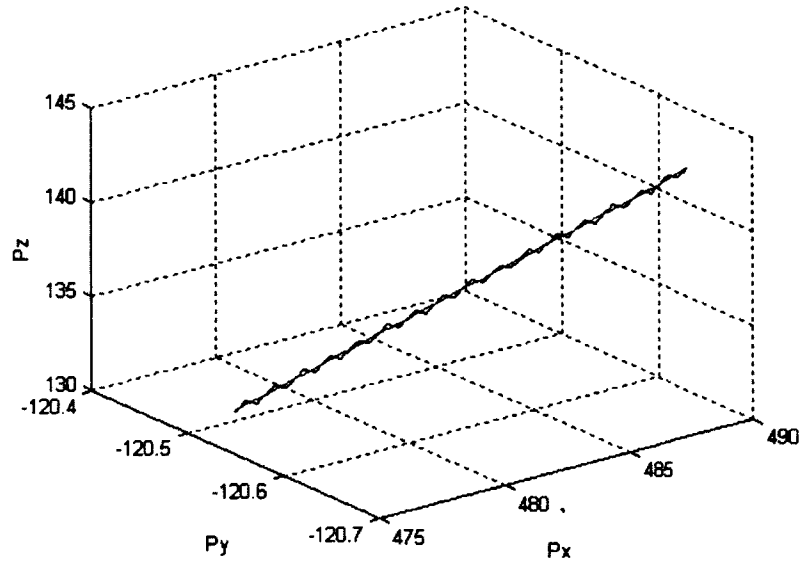

Figure 4.7 Robot Arm Current Position Trajectory for the Straight Line Motion

4.3 Robot Motion Algorithm

In this section, robot motion algorithms for the trajectories generated from section 4.2 were provided. The following algorithms were developed for the different types of drilling procedures. When the robot starts to mill out the hole on the object, thermal effect is the most important issue. Thus, for the straight line drilling path we considered backward feeding movement of the robot instead of only considering forward drilling directly so that human bone structure can be guarded from the high thermal effect. In the straight line algorithm, p_f and p_b denote the forward and backward robot movements, respectively. Therefore, the robot performs the positioning with respect to the constrained depth, l_b. Through the algorithms, robotic milling constraints derived in section 2.3 were implemented at each function.

Define straight line path : Algorithm 1

for l = 0: step: dist(p,t)

$$\left.\begin{aligned} x_f &= p_x - l(\sin\phi \sin\psi + \cos\phi \sin\theta \cos\psi)\bullet \mathrm{sign}(x_f - p_x) \\ y_f &= p_y - l(\cos\phi \sin\theta \sin\psi - \sin\phi \cos\psi)\bullet \mathrm{sign}(y_f - p_y) \\ z_f &= p_z - l(\cos\phi \cos\theta)\bullet \mathrm{sign}(z_f - p_z) \end{aligned}\right\} p_f(x_f,y_f,z_f)$$

$$\left.\begin{aligned} x_b &= x_f + l_b(\sin\phi \sin\psi + \cos\phi \sin\theta \cos\psi)\bullet \mathrm{sign}(x_f - p_x) \\ y_b &= y_f + l_b (\cos\phi \sin\theta \sin\psi - \sin\phi \cos\psi)\bullet \mathrm{sign}(y_f - p_y) \\ z_b &= z_f + l_b (\cos\phi \cos\theta)\bullet \mathrm{sign}(z_f - p_z) \end{aligned}\right\} p_b(x_b,y_b,z_b)$$

if $l \le l_b$ **then** perform robot movement

move $p_f(x_f,y_f,z_f)$

break

l_b = constrained depth

else if **then** perform robot movement

move $p_f(x_f,y_f,z_f)$

move $p_b(x_b,y_b,z_b)$

break

end

call: subconstraints(p,p_f,p_b) – check area constraints

end

Algorithm 2 describes the trajectory functions with respect to the geometric volume. A user can call the volume type for the robot drilling with predefined parameters given in the functions. However, functions called mvtooth1 and mvtooth2 only deal with a point cloud data set composed of single-root and double-root implant shapes. Based on the data size of each root, robot drilling operation time can be increased or decreased.

Choose geometrical shape for drilling: Algorithm 2

Select: geometrical type

case 1

call: mvcylinder(r, h, ϕ, θ, ψ, step, p_{target})

break

case 2

call: mvcone(r, h, ϕ, θ, ψ, step, p_{target})

break

case 3

call: mvellip(a_{max}, b_{max}, h, β, ϕ, θ, ψ, step, p_{target})

break

case 4

call: mvtellip(a_{max}, a_{min}, b_{max}, h, β, ϕ, θ, ψ, step, p_{target})

break

case 5

call: mvtooth1(a point cloud data set for single-root implant)

break

case 6

call: mvtooth2(a point cloud data set for double-root implant)

break

end

Algorithm 3 specifically illustrates the subroutines of different types of volumes in terms of parameters. Each subroutine initializes the target pose before starting the milling process for alignment of the tool tip's orientation to target position. Note, parameter step provides the step size of the volumetric depth.

Subroutine : Algorithm 3

mvcylinder(r, h, ϕ, θ, ψ, step, p_{target}): subroutine for cylinder

```
p_cylinder = initialize(p_target)
for r = 0:step: R
    for α = 0:step:2π
        x = rcosα
        y = rsinα
        z = 0
        p_cylinder = f(α, φ, θ, ψ, x, y,z)
        move p_cylinder: perform robot movement
    end
end
```

mvcone(r, h, ϕ, θ, ψ, step, p_{target}): subroutine for cone

```
p_cone = initialize(p_target)
for r = 0:step: R
    for α = 0:step:2π
        x = rcosα
        y = rsinα
        z = r(h/R)
        p_cone = f(α, φ, θ, ψ, x, y, z)
        move p_cone: perform robot movement
    end
end
```

mvellip(a_{max}, b_{max}, h, β, ϕ,θ, ψ, step, p_{target}): subroutine for elliptic cone

```
p_elliptic = initialize(p_target)
e = sqrt((a_max^2 – b_max^2)/a_max^2)
for a = 0:step:a_max
    b = sqrt(a^2(1-e^2))
    for α = 0:step:2π
```

```
        x = acosαcosβ - bsinαsinβ
        y = a cosαsinβ + bsinαcosβ
        z = a(h/a_max)
        p_elliptic = f(a, b, h, β, ϕ, θ, ψ, x, y,z)
        move p_elliptic: perform robot movement
    end
end
```

<u>mvtellip(a_{max}, a_{min}, b_{max}, h, β, ϕ,θ, ψ , step, p_{target}): subroutine for elliptic frustum</u>

```
p_telliptic = initialize(p_target)
e = sqrt((a_max^2 – b_max^2)/a_max^2)
for a = 0:step:amax
    b = sqrt(a^2(1-e^2))
    if a ≤ a_min then
        for α = 0:step:2π
          p_telliptic = f(a, b, h, β, ϕ, θ, ψ, x, y,z)
          move p_telliptic: perform robot movement
        end
    else if
        for α = 0:step:2π
          x = acosαcosβ - bsinαsinβ
          y = acosαsinβ + bsinαcosβ
          z = (a – a_min)(h/(a_max – a_min))
          p_telliptic = f(a, b, h, β, ϕ, θ, ψ, x, y,z)
          move p_telliptic: perform robot movement
        end
    end
end
```

Evaluation of Phantom experiments was carried out to evaluate the efficiency of utilizing two different milling strategies (see Figures 4.8 – 4.9). Two types of milling sequences were considered to compare the milling time based on geometry. One was a point cloud sequence, and the other used subroutines defined by geometrical volumes. Table 4.1

shows that the drilling duration using subroutines cone, cylinder and elliptic cone were 100.17, 291.49 and 130.57 seconds, while those of the point cloud milling sequence were 311.33, 55.84, 403.25 seconds, respectively. From these results, drilling time using subroutines was about 3 times shorter than that of the point cloud sequence method. However, for the cylinder case, it took 5 times less than the subroutine due to the significantly smaller data size compared to other volumes. These results will be used in future work to examine the performances with regards to natural-root form implant shapes.

Figure 4.8 Robotic Milling in the Jaw Model

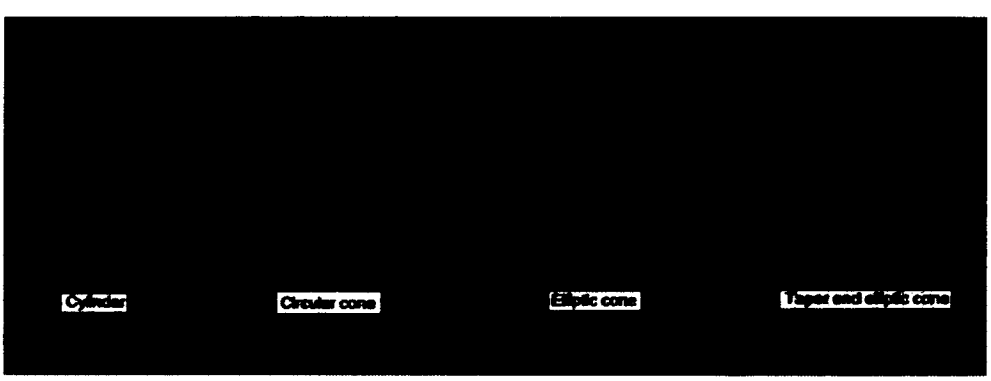

Figure 4.9 Robotic Milling for Different Types of Volumes Using Subroutines

Table 4.1 Speedy Test for Two Different Milling Sequences

Geometry Type	Parameters	Point Cloud		Volume Decomposition	
		Drilling Time (sec)	Data size	Drilling Time (sec)	Data size
Cone	V = 2 mm/s, r=3, h=6, step=0.1	311.33	2488	100.17	N/A
Cylinder	V = 2 mm/s, r=3, h=6, step=0.1	55.84	436	291.49	N/A
Elliptic Cone	V=2, a1=4,b1=3,a2=2.83	403.25	3094	130.57	N/A

4.4 Vibration Test

4.4.1 Overview of Experimental Setup

Since the robot performs the drilling on the hard or soft material, there is a possibility that the vibration mode on the dental tool may affect the hole-shapes. In this section, we assume that the dental tool was rigidly attached to the robot end-effector. Thus, a single-axis accelerometer attached to the dental handpiece toward the *z*-direction was used to measure the vibration behavior during the robotic drilling process, and we investigated how this vibration mode affected the milling process.

The installation of the sensor and the implementation of the data acquisition system are displayed in Figure 4.10. A single-axis PCB accelerometer was attached to the dental tool to collect the vibration data using the data acquisition device powered by the Quattro hardware module. Measurement and analysis was performed using a Data Physics SignalCalc ACE dynamic signal analyzer and Matlab R2008b. During the data sampling, the dental drill-bit speed and torque were constrained as 1500 rpm and 20 N-cm, respectively.

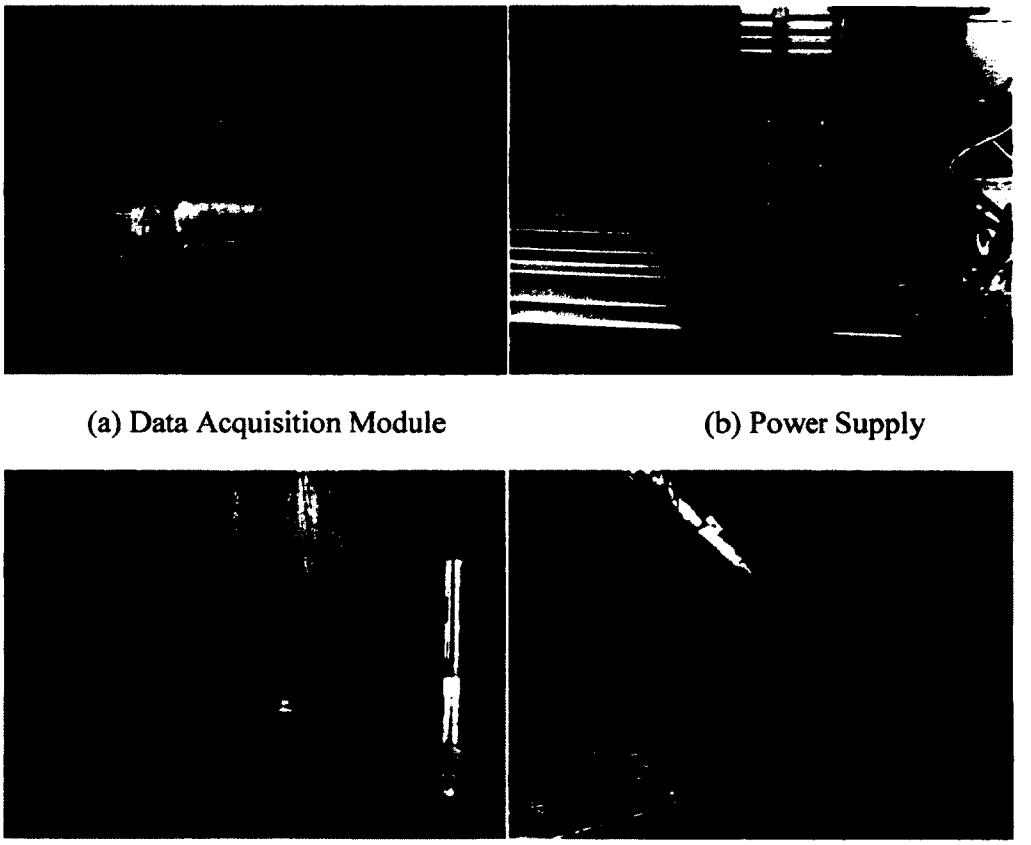

(a) Data Acquisition Module (b) Power Supply

(c) Electric Hammer (d) Single-Axis Accelerometer

Figure 4.10 Data Acquisition Module for Vibration Test

Initially, in order to generate the vibration signal on the dental drill-bit, the pressure pedal in the dental tool unit was operated at the same rpm and torque. In this test, only a straight drilling process was considered since only a single-axis sensor was available.

The acceleration signals were measured five times, and we took the mean value of them. The Z direction of the accelerometer sensor aligned with the downward direction. Data collection was performed under 80 Hz sampling frequency over 10 seconds. The total collected data size was 4096. A second order Butterworth low pass filter was used to cancel out the noise (see Equation 4.16).

$$P(s) = \frac{1}{s^2 + 1.414s + 1} \tag{4.16}$$

Figure 4.11 shows how the acceleration for the z-axis varies with drilling time and the filtered data which follows the original data's characteristics.

In Figure 4.12, the Fast Fourier transform of the filtered signal shows that obvious peaks were found near 1 Hz, 62Hz and 75 Hz with cut-off frequency of 5 Hz, in semi-log scale for the Z-direction. However, in real scale, there was no obvious peak in the frequency range, while the signal distribution is random in the semi-log scale. Since a single-axis accelerometer was used in the Z-direction for vibration, this result limits the use of X and Y-directions. However, the result shows that the vibration mode of the robot tool-tip provides almost constant deviation for the milling operation.

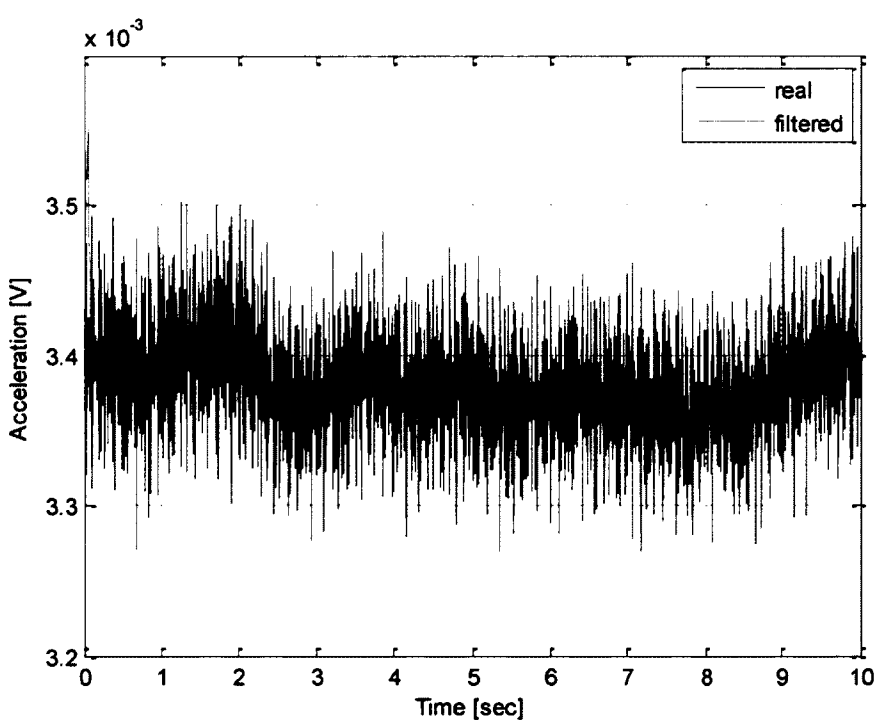

Figure 4.11 Real Time Vibration Signal in Z Direction

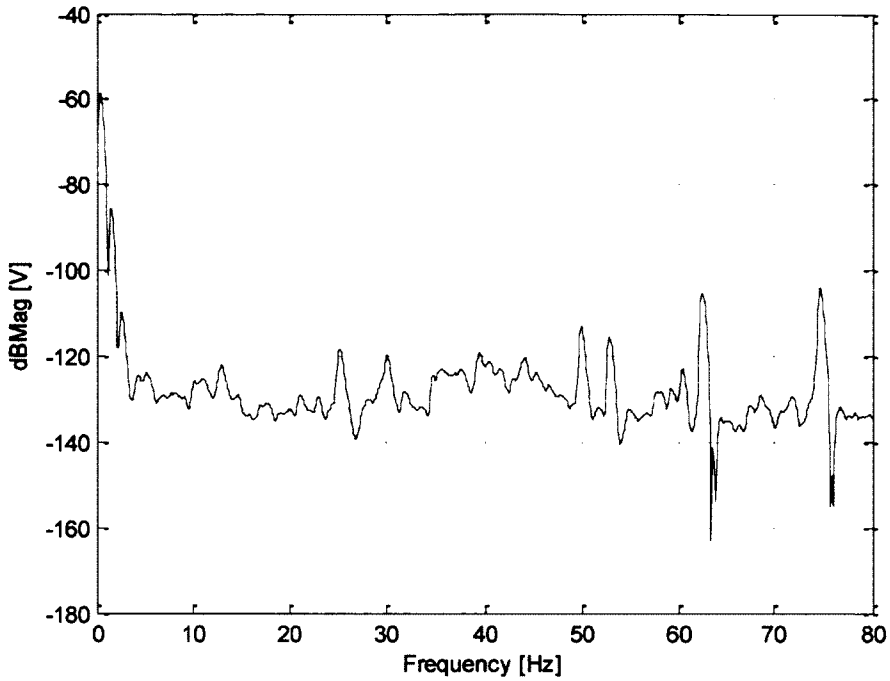

Figure 4.12 Auto Power Spectrum in Semi Log Scale for the Magnitude

CHAPTER 5

SYSTEM OVERVIEW

5.1 System Architecture Overview

This section describes the development of an image-guided autonomous robotic milling system based on different types of volume removal that also incorporates natural root-shaped implants. This new framework offers significant potential for precise milling processes when compared to a conventional approach. Also, utilization of the GUI tool for operation of robotic surgery that goes beyond baseline control architectures typically generated with open-loop design strategies is introduced.

Figures 5.1 – 5.2 outline the software and programmable robotic architectures. In Figure 5.1, dental implant models composed of volumetric data were generated using a volume decomposition program. This volume information implemented in the MELFA script is transferred to the robot controller. In the MELFA main script file, a user can call subroutines with respect to the implant shapes and robotic motion constraints. Thus, one can execute the robot to perform the surgical operation.

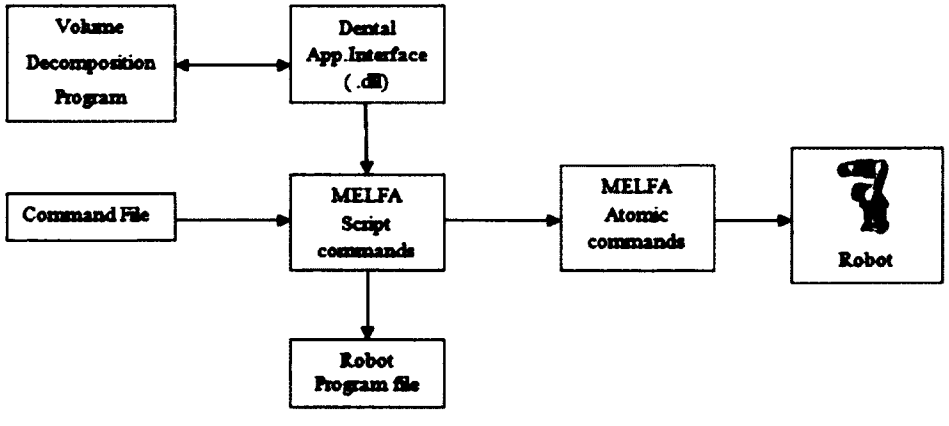

Figure 5.1 Software Architecture

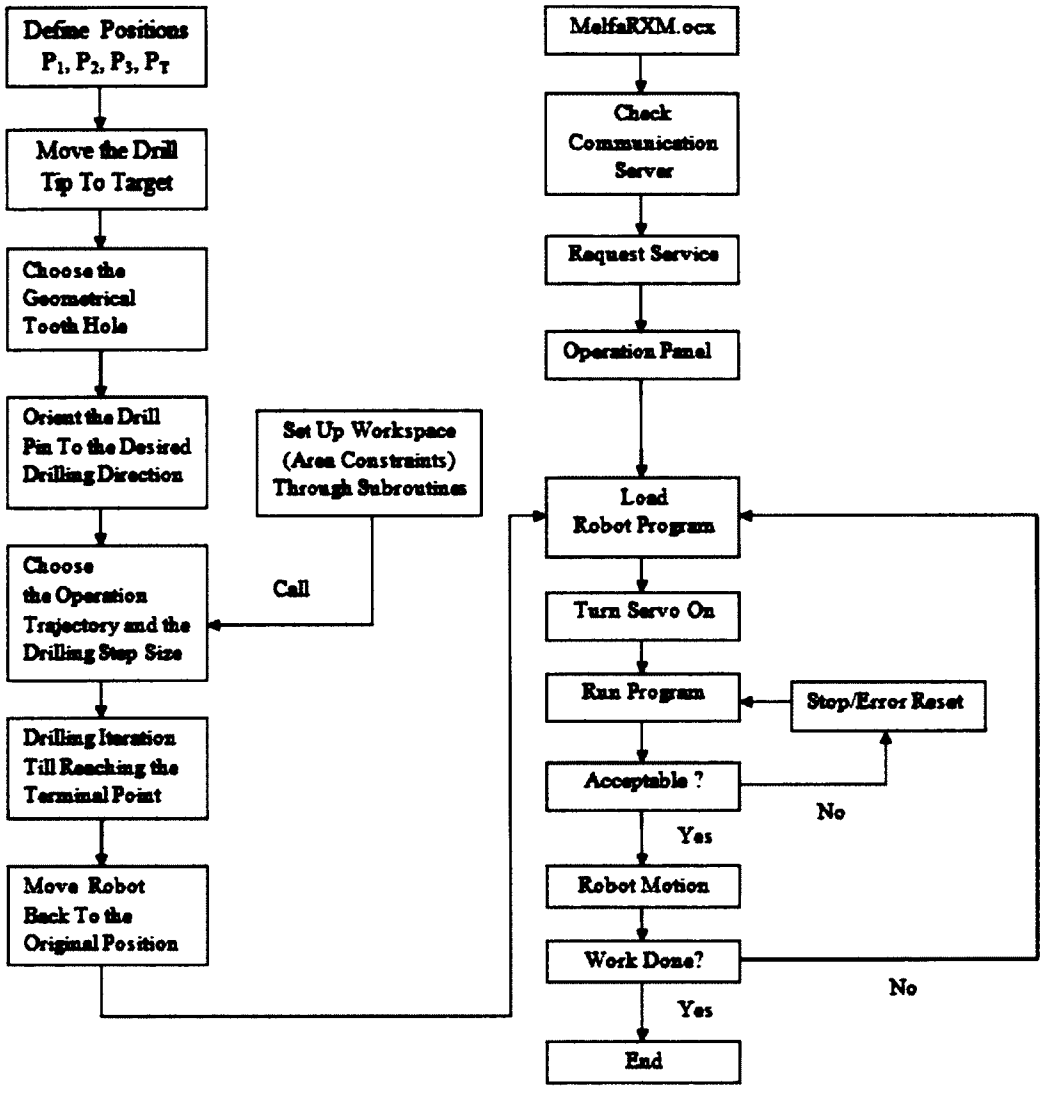

Figure 5.2 Implementation and Usage Flow Chart

5.2 Hardware Architecture

Figure 5.3 shows the overall system flow chart including pre-operative planning and an intra-operative part. For greater detail of the robotic milling site, hardware architecture in the operation coordinate system is considered in Figure 5.4. The robotic milling system is composed of a Mitsubishi Electric Factory Automation (MELFA) RV-3S robot with a

RS232 communication port and Dell 600 Vista operation system. The dental drill unit was attached to the robot end-effector for milling of the bone structure. The two-way interface for the robot provides the current operating parameters of the robot via the robot control unit as well as a command interface for manipulator control.

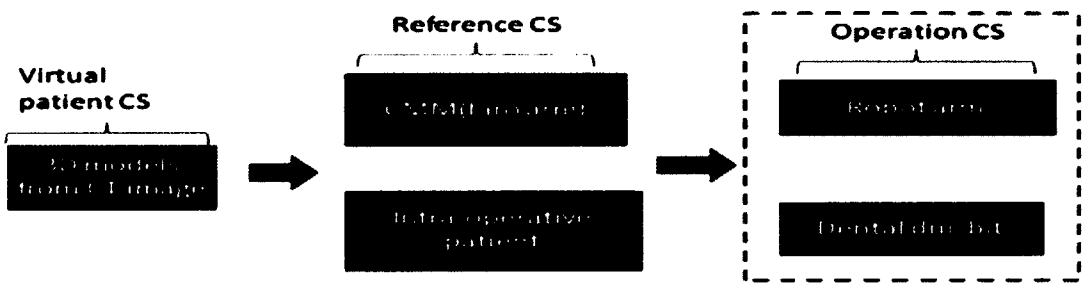

Figure 5.3 Overall System Flow Chart

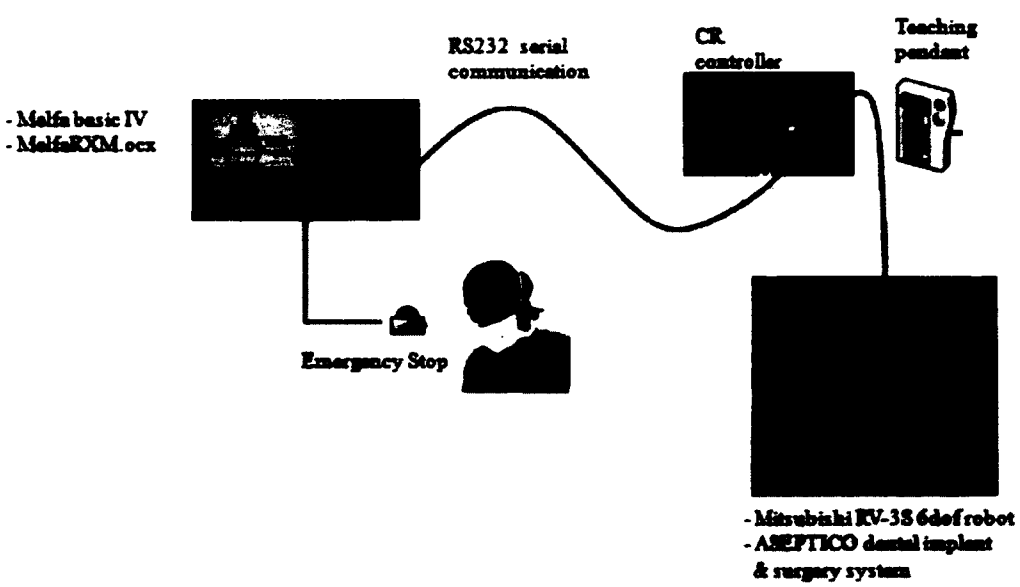

Figure 5.4 Hardware Architecture

5.3 GUI Tool Utilization

Five different types of volume milling algorithms were implemented in the MELFA robot controller: specifically cone, cylinder, elliptic cone, elliptic frustum, and natural tooth-shaped volume. All the subroutines created for different volumes can be called through the MELFARXM GUI panel, which is an ActiveX based GUI, to perform the operation in Figure 5.5. As seen in the figure, a user is allowed to execute a mouse-clicking operation from the personal computer at the user site. This GUI panel contains: (1) robot servo on and off switch, (2) program start and stop, (3) emergency stop and error reset. In this manner, a user can send and receive messages and data into the robot controller (see Figure 5.6). The communication server performs transmission processing and sends requests to the robot controller. Thus, when MELFARXM.ocx receives a transmission message, a reception event occurs. This process goes on to get data from the robot controller via the communication process.

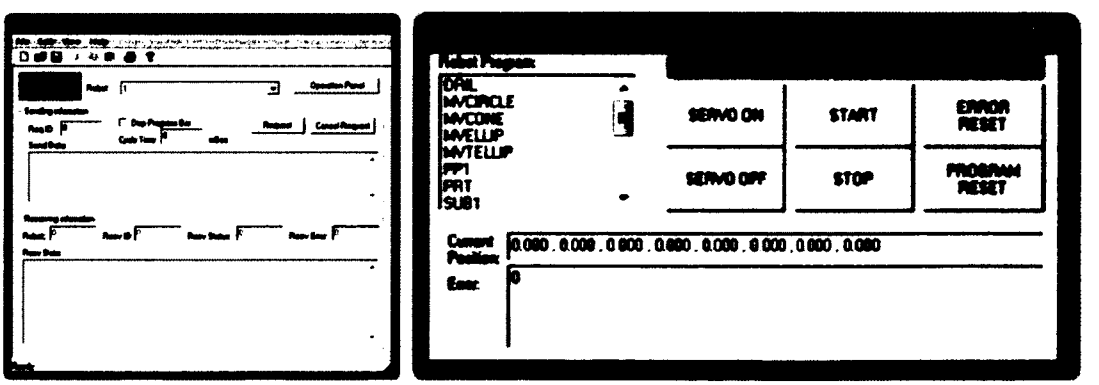

Figure 5.5 MELFARXM GUI Tool

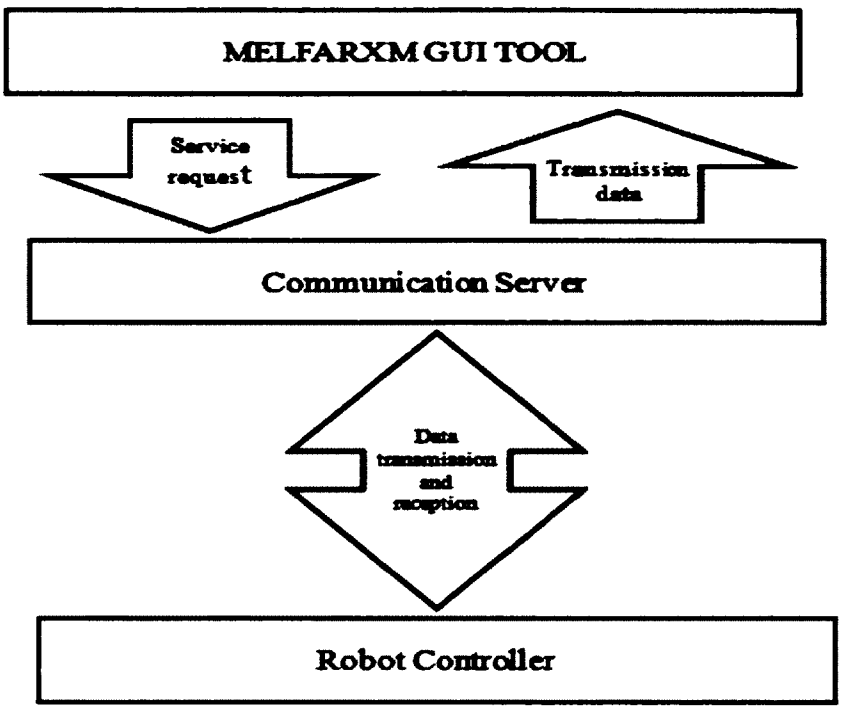

Figure 5.6 MELFARXM Layout

CHAPTER 6
TOPOLOGY OPTIMIZATION OF DENTAL IMPLANT

6.1 Introductory Remark

A simplified model of an implant was created based on several assumptions. This simplified mandibular segment with an implant was also modeled using MD Patran 2010. The first step of the modeling was to define the bone and implant geometry. This is followed by specifying the material behavior in terms of the Young's modulus, Poisson's ratio and density for various mandibular bone components and the implant. After applying the load and boundary conditions, the various parameters and their contributions to the stress profile can be evaluated. Figure 6.1 illustrates the overall view of the natural tooth and dental implant in the current clinical process.

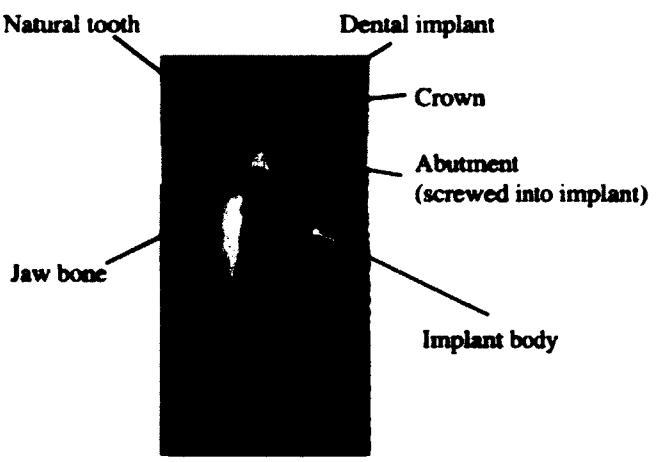

Figure 6.1 Cross-Sectional View of a Natural Tooth and a Dental Implant [3]

6.2 Preliminary Design with 2D Model

FEA has become one of the popular analysis methods to solve dental related Bioengineering problems. Due to complex geometry, certain assumptions need to be made in dealing with complicated implant, jawbone and implant-jawbone interaction problems[3]. Five assumptions were used based on reference [3]:

(1) The simplified 2D geometric model of the implant and jawbone structures is employed based on certain assumptions;

(2) Instead of using dynamic loading, static loading on the structure is considered due to computation time and the model structure simplification;

(3) Since it is hard to model the standard jawbone structure for different patients, the interface between the jawbone and the implant are considered as perfectly bonded;

(4) Bone structure (cortical and cancellous bones) in the mandibular region is characterized as homogeneous, linearly elastic material defined by each Young's modulus and Poisson's ratio;

(5) A cylinder shape of implant is employed.

Material properties such as Young's modulus and Poisson's ratio greatly influence the stress and strain distribution in a dental structure. These properties can be implemented in FEA as isotropic, orthotropic, and anisotropic based on material types. Since material properties are different among the bones and implant, materials composed of jawbone can be determined by two independent variables, Young's modulus and Poisson's ratio, in isotropic material. Figure 6.2 shows the simplified bone and implant geometry of a 2D

model with the loading and boundary conditions. In the 2D model, the structure was characterized using a plain-strain condition. The cancellous bone was surrounded by 1 *mm* thick cortical bone. The total numbers of elements are 645, and the ones of nodal points in the entire model are 718. For a 2D case, only 200N axial force was applied to the top surface of the implant. As seen in Figure 6.2, both sides of the model are restrained for the x component, while all the degrees of freedom for the bottom face of the bone are zero. A press-fit implant was modeled, and it is assumed that the bone and implant were bonded perfectly along their interface. Since the investigation of stress distribution around the implant neck is the main purpose, the bottom layer of the cortical bone was not modeled. Material properties were employed from Table 6.1.

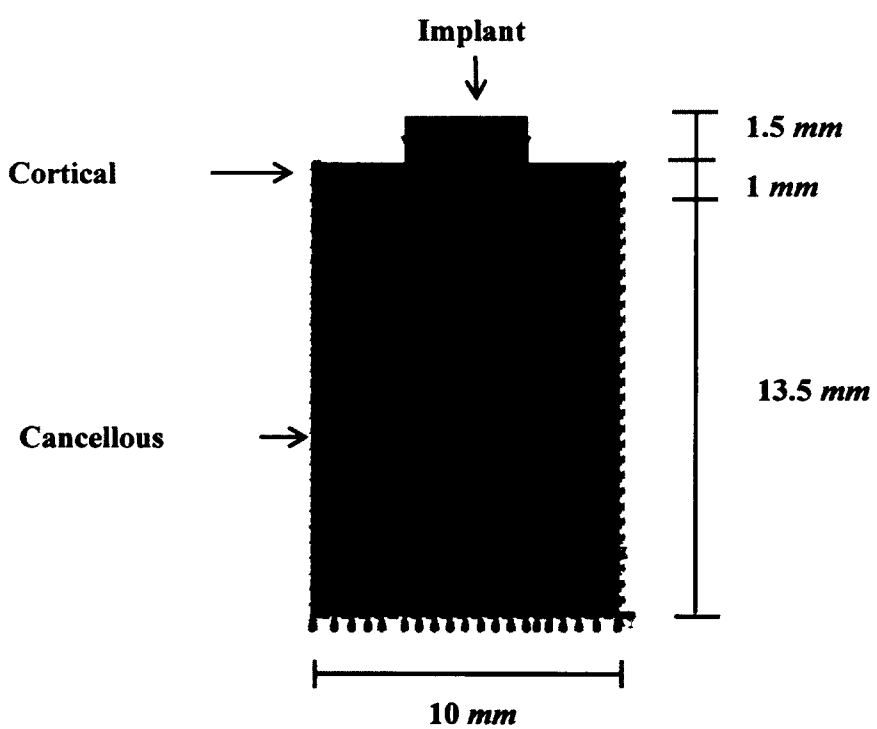

Figure 6.2 2D Dental Implant Specification

Table 6.1 Material Properties [50]

Materials	Young's Modulus (GPa)	Poisson's Ratio
Cortical Bone	13.7	0.3
Cancellous Bone	7.55	0.3
Implant(titanium)	110	0.33

Contours of Von Mises stress under axial load of 200N are shown in Figure 6.3. In the cortical and implant interface (see Figure 3), a high level of Von Mises stress exists near the bone around the implant neck, and the magnitude of stress is decreased along the cortical bone from 12.9 MPa to 8.3MPa which is in reasonable rage compared to the result of the reference [50]. The von Mises stresses recorded at the cortical bone are plotted against the insertion depth in Figure 6.4. In reality, 2D finite element analysis is not enough to investigate the stress level of the dental model since the implant has a cylindrical shape. Thus, a 3D model is used to perform more accurate finite element analysis.

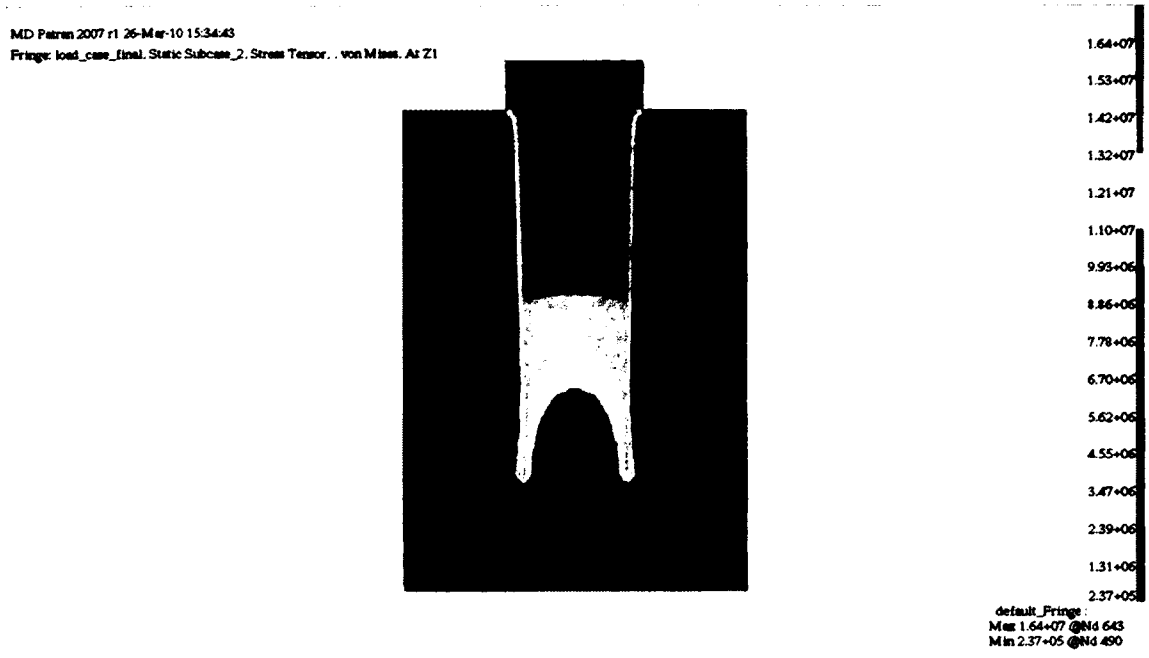

Figure 6.3 Contour Level of Von Mises Stress Under an Axial Loading

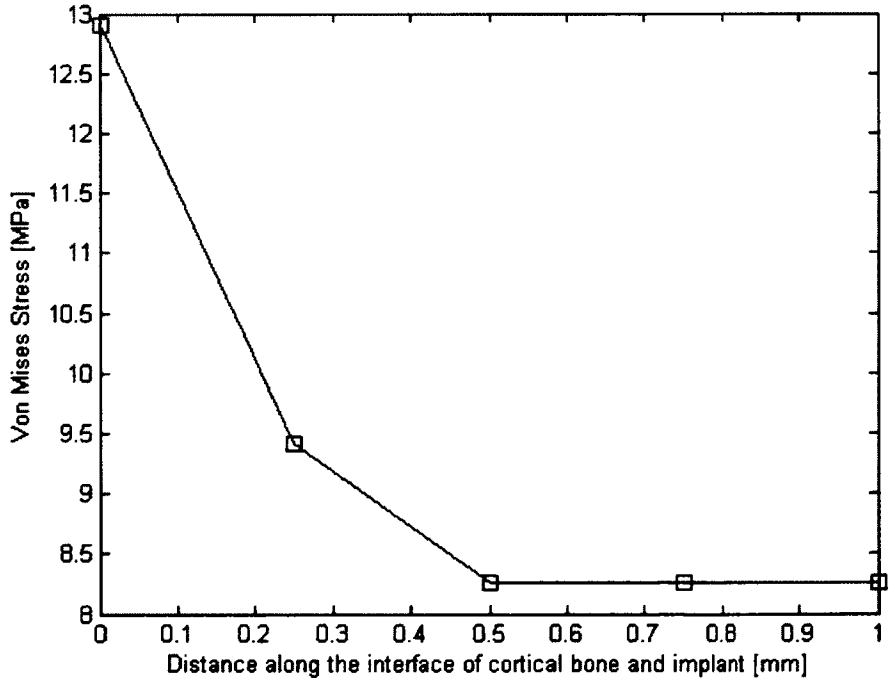

Figure 6.4 Von Mises Stress vs. Depth Along the Interface of Cortical Bone And Implant

6.3 Preliminary Design with 3D Model

In 3D preliminary analysis, the stress and strain are evaluated in all directions. The first step in 3D FEA modeling is to represent the geometry of interest in the dental model. Stress distribution depends on assumptions made in geometry, material properties, boundary conditions, and the bone-implant interface. In this section, the mandible was treated as an arch with a simplified rectangular section as cancellous bone surrounded by a 1 mm thick cortical layer, and the overall dimensions of this block were 15.5 mm in height, 10 mm in mesiodistal length, and 10 mm in buccolingual width in the 3D FEA model (see Figure 6.5). An implant with a height of 13 *mm* was used to model a cylindrical implant with 2 mm of radius. For simplicity, the screw thread was not modeled, and it is assumed that the bone and implant were bonded perfectly along their interface. Due to geometrical symmetry, a half model was used for the FEM analysis.

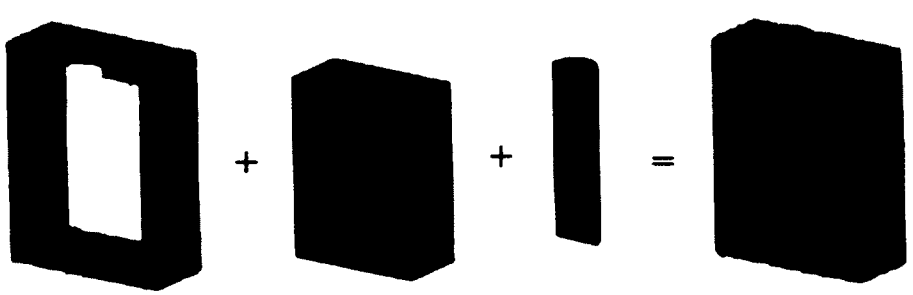

a. Cortical Bone b. Cancellous Bone c. Implant d. Half Model

Figure 6.5 3D Dental Implant Model

All materials used in this model are the same as the 2D model. The 3D FEA model was meshed with 8-node-hexahedron elements composed of 16977 elements and 19363 nodes. 200N of axial load was applied to the top surface of the implant. Figure 6.6

illustrates the boundary conditions with 200N of axial and oblique loads separately on the top surface of the implant. All degrees of freedom on the bottom face are constrained, while a mirror plane is constrained only for the y-component.

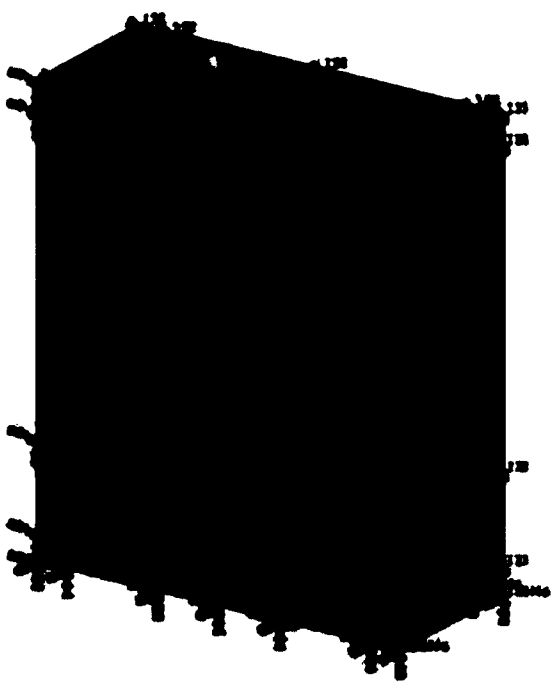

Figure 6.6 Loading and Boundary Conditions in 3D Dental Model

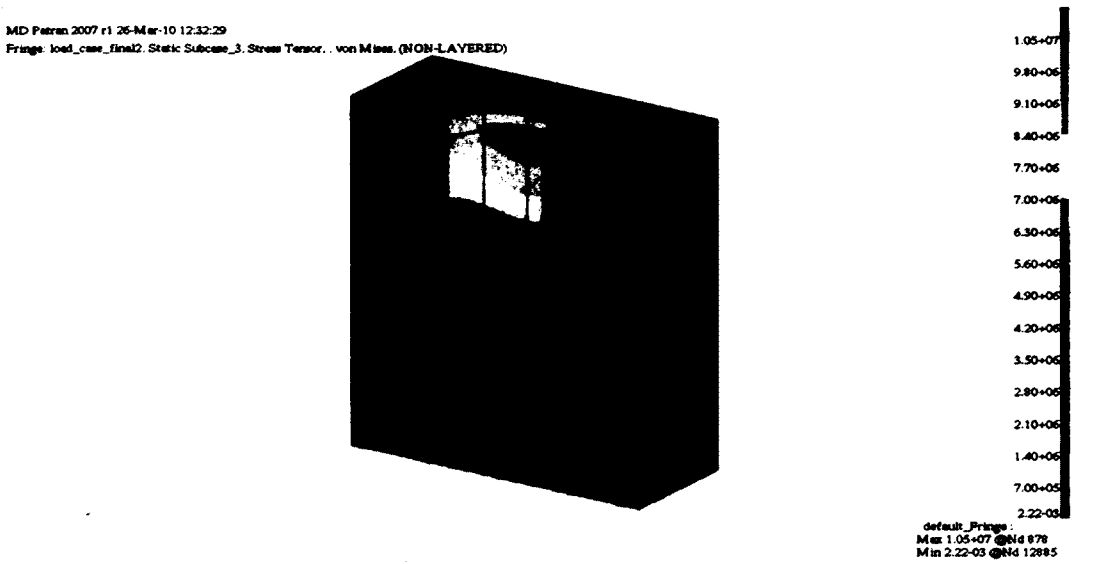

Figure 6.7 Contour Level of Von Mises Stress Under An Axial Loading for Half Model

The maximum stress is concentrated at the interface between the cortical bone and implant area as seen in the 2D results (see Figures 6.7- 6.8). Figure 6.9 shows Von Mises stress distribution along the interface of the cortical bone and implant for the 2D and 3D models. The stress level of the 3D FEA model under 200 N of total load on the top surface was dropped down compared to the 2D model, since the compressive stresses around the neck interface for both models dissipated radially from the loading area, which means that the 3D model has a wider loading area to dissipate the stress.

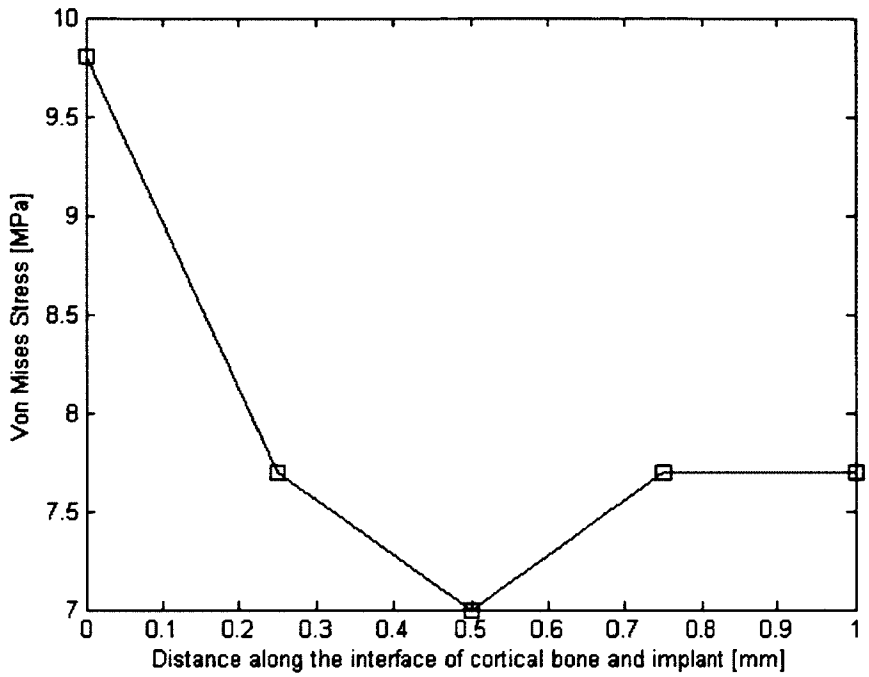

Figure 6.8 Von Mises Stress vs. Distance Along The Interface of Cortical Bone And Implant

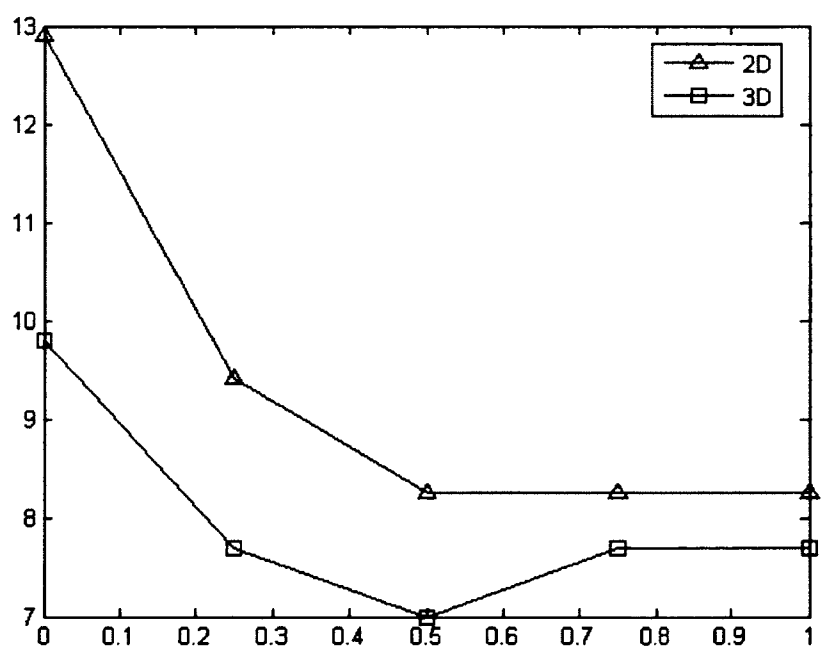

Figure 6.9 Von Mises Stress Along The Path Length for 2D and 3D

For further study, a two-root natural tooth FEA model was created to compare how natural roots influence the stress level compared to the cylinder shape implants. Figure 6.10 provides basic information about the maximum stress level for both models. One can see that the natural tooth shape tends to have significantly less maximum stress along the interface of the bone and implant due to a larger surface area for the loading condition. Note that Figure 6.10 only considers maximum Von Mises stresses.

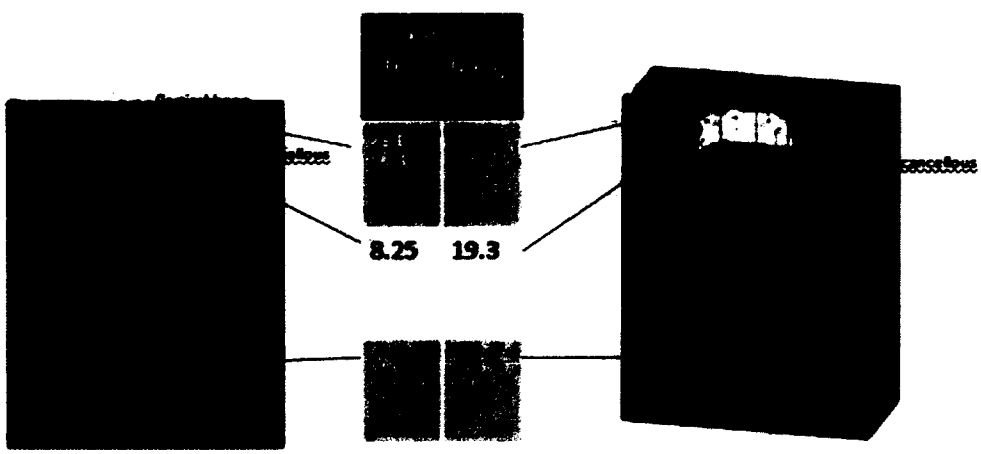

(a) Natural Root (b) Implant

Figure 6.10 Comparison of Stress Level Between Natural Tooth and Implant

6.4 Methodology – SKO Optimization

Topology optimization is widely used in applications where the weight of an object needs to be reduced to a minimum. The main principle in topology optimization is that the material layout should be optimized within a given design domain using a mathematical approach. The procedure of topology optimization starts with a design space that will be reduced to the final solution. The design space limits the solution and should be larger

than the predicted solution. The simplest category of algorithms uses the stress to find the regions where the material is useful and where it is not. In this study, the SKO method, one of the topology optimization techniques was used [51]. Many topology optimization methods start with a design space, which is filled with material with a certain density, $0 \leq \rho \leq 1$. However, the SKO method starts with $\rho=1$ and then changes the material under the design parameters and constraints. It does not keep the mass of the design constant, but it will keep the minimum stress of the design constant. The materials used for the design space in this study have the following properties: Young's Modulus (E=1.37 GPa, 13.7 GPa), and Poisson's ratio ($\upsilon=0.3$).

6.4.1 Overview of the Simulation

Figure 6.11 illustrates the general concept of the topology optimization process. The model was created and analyzed with the following steps using FE software, ABAQUS/CAE/STANDARD. Firstly, a FE model was created by Patran 2010 and then converted to an ABAQUS input file for the SKO optimization. In order to update the Young's modulus, a user defined material subroutine (UMAT) was used to define the mechanical constitutive behavior of two different materials – cortical and cancellous bone - while the implant has a constant material property. The UMAT subroutine updates the stresses and solution-dependent state variables at the end of the increment which can provide the material Jacobian matrix for the model. A FORTRAN environment is set up to manage the interaction between the ABAQUS input file and the UMAT subroutine.

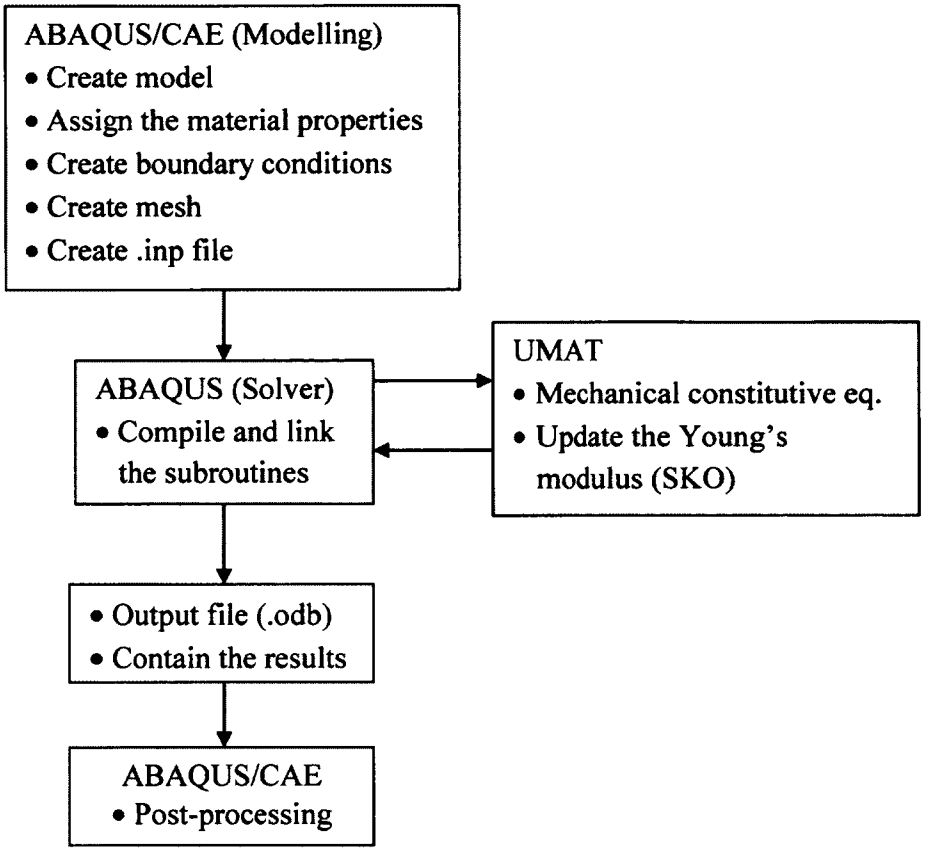

Figure 6.11 Diagram of Optimization Process

6.4.2 Topology Optimization Using Soft Kill Option (SKO)

The SKO optimizing process [51] iterates in order to find the optimal solution as illustrated in Figure 6.12. The process was started with both the anatomically correct model and the model that was refined for robotic milling. The stresses are evaluated in each iteration and depending on the stress level in the elements, the elastic modulus is adjusted. Elements with high stresses are made a bit stiffer before the next iteration and vice versa. The steps are as follows:

- Start with a design space and fill it with finite elements. The user should select which

material will be assigned in each iteration during computation if there are several materials;

- Generate a FEM-simulation and check the stresses in the part;
- Let each element's material stiffness be a function of the stress in the previous iteration

  $E_{i+1} = f(\sigma_i)$ (Equation (6.5));
- Check the convergence of Young's modulus; Step 2 and 3 should be repeated until the process converges;
- Optimize the solution.

One can also introduce a global reference stress, σ_{ref}, for the entire model. Eqn. (2.1) was employed to update the Young's modulus in design space.

$$E_{i+1} = E_i + k(\sigma_i - \sigma_{ref}) \tag{6.1}$$

In Equation (6.1), global reference stress, σ_{ref}, controls the variation of the Young's modulus and k is a positive scaling factor to adjust the speed of the process to update the Young's modulus. In this study, three different materials were considered: implant, cortical bone, and cancellous bone. Thus, one has to limit the Young's modulus such as $E \in [E_{min}, E_{max}]$

$$\text{i.e.} \quad \begin{aligned} E_{i+1} &= E_{min} \quad \textit{if } E_{i+1} < E_{min} \\ E_{i+1} &= E_{max} \quad ; \textit{otherwise}, \end{aligned} \tag{6.2}$$

where E_{min} denotes either cortical bone or cancellous bone, and E_{max} denotes the implant. In this way, a reasonable scaling factor, k, will be calculated as follows:

$$k = \frac{(E_{max} - E_{min})}{\sigma_{ref}} . \tag{6.3}$$

In this research, the reference stress in Equation (6.1) is compared with the stress calculated in the 3D model as the von Mises stress using Eqn. (6.4) which is implemented in the UMAT subroutine.

$$\sigma_{VM} = \sqrt{\frac{(\sigma_1-\sigma_2)^2+(\sigma_2-\sigma_3)^2+(\sigma_1-\sigma_3)^2+6(\sigma_{12}{}^2+\sigma_{23}{}^2+\sigma_{13}{}^2)}{2}} \tag{6.4}$$

It is more effective to start using a lower value for the reference stress and then increase it slowly from cycle to cycle until the process converges under the design constraints indicated in Equation (6.5).

Section 6.5 studies the effect of the local Young's modulus gradation in the 2D and 3D jawbone subject to a uniform axial loading on the top surface of the implant. The modulus was graded in the z direction emanating from the contact surface between implant specimen and cortical bone into the section toward the outer traction boundaries. In the UMAT subroutine, the Young's modulus was varied starting at the contact surface between implant and cortical bone but now was limited in depth such that gradation did not extend to the outer boundaries (except for the initial run to establish a baseline). The goal was to create the optimized Young's modulus to reduce the magnitude of stress concentration for both the anatomically correct models and the refined models.

$$\begin{bmatrix}\sigma_{xx}\\ \sigma_{yy}\\ \sigma_{zz}\\ \sigma_{yz}\\ \sigma_{zx}\\ \sigma_{xy}\end{bmatrix} = \frac{E}{(1+\nu)(1-2\nu)}\begin{bmatrix}1-\nu & \nu & \nu & 0 & 0 & 0\\ \nu & 1-\nu & \nu & 0 & 0 & 0\\ \nu & \nu & 1-\nu & 0 & 0 & 0\\ 0 & 0 & 0 & 1-2\nu & 0 & 0\\ 0 & 0 & 0 & 0 & 1-2\nu & 0\\ 0 & 0 & 0 & 0 & 0 & 1-2\nu\end{bmatrix}\begin{bmatrix}\varepsilon_{xx}\\ \varepsilon_{yy}\\ \varepsilon_{zz}\\ \varepsilon_{yz}\\ \varepsilon_{zx}\\ \varepsilon_{xy}\end{bmatrix} \tag{6.5}$$

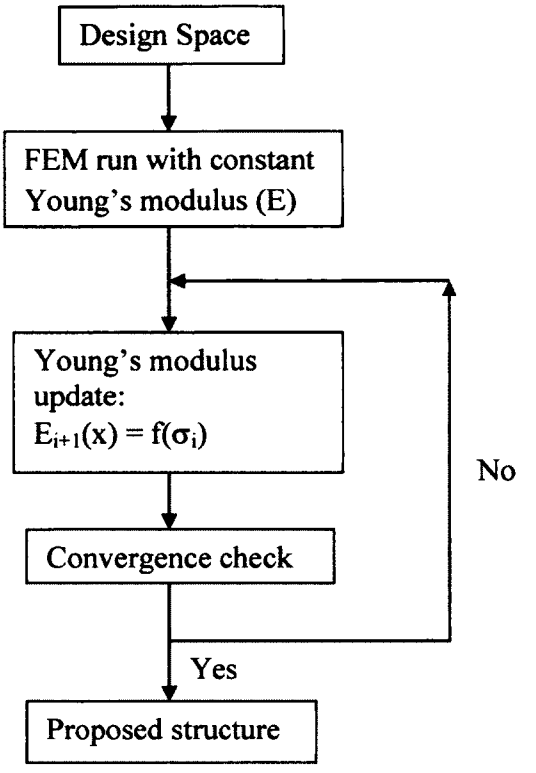

Figure 6.12 Flowchart of the SKO

6.4.3 Algorithm of the UMAT

The main objectives of UMAT are as follows:

1) Update the stress;

2) Obtain Jacobian matrix.

A general process for the update of solution dependant variables (SDV) in ABAQUS, is given as follows. For the given variables (σ, ε, $\Delta\varepsilon$), at the start of the initial step UMAT calculates the σ , ε , and SDVs, and transfers the Jacobian matrix for a global iterative Newton-Raphson solution. Figure 6.13 shows the flow chart of the UMAT implementation. For the initialization process, one has to select which material will be assigned each iteration during computation if there are several materials. Then a

mechanical constitutive equation (see Equation (6.5)) will be defined to form the elastic stiffness matrix. Based on this information, stress and state variables (Young's Modulus for this research) will be updated.

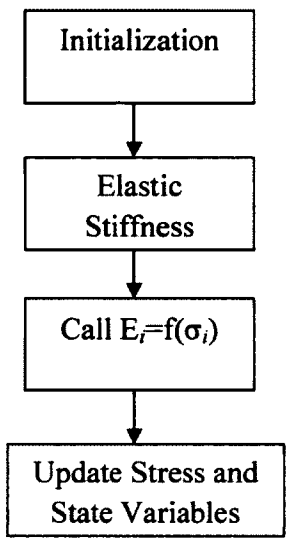

Figure 6.13 Flowchart of UMAT Implementation

To model the solution dependent Young's modulus in this study, the ABAQUS user material subroutine (UMAT) was used. The subroutine, which was written in FORTRAN, runs with the Abaqus solver. Thus, the user can establish an algorithm to calculate solution dependant state variables. In this way the subroutine was coded such that the material and stiffness matrices were implemented with the state variable, i.e., Young's modulus. Poisson's ratio was assumed to be constant due to significantly less variation compared to Young's modulus. The method required for establishing the stiffness matrix requires Equation (6.1) to be integrated numerically.

The following section studies the effect of the local Young's modulus gradation in the 2D jawbone subject to a uniform axial loading on the top surface of the implant. The

modulus was graded in the y direction emanating from the contact surface between the implant specimen and cortical bone into the section toward the outer traction boundaries. In the user material subroutine, Young's modulus was varied starting at the contact surface between implant and cortical bone, but now it was limited in depth such that gradation did not cover the outer boundary. The goal was to find an optimized shape of the implant to reduce the magnitude of stress concentration.

6.5 Simulation Results – 2D FEA Model

6.5.1 Initial Design

Figure 6.14 Initial Design Domain

In Figure 6.14, 2D mesh was generated using eight-node plain-strain elements with 10 *mm* thickness. Considering von Mises stress as the results, non-zero σ_{33} is needed to constrain ε_{33} for the 2D model. In this 2D model, 1880 quadratic (CPE8) elements and 5839 nodes were contained with 200 N of axial force on the central node at the titanium specimen. Figure 6.15 shows the simulated results using the SKO method. As seen,

reference stress lower than 2MPa (a-b) led the model to have the tooth with one root. When the reference stress is more than the 2.5MPa (c), it has a tendency to become a natural tooth with two roots. As the reference stress was increased, the width of the implant tapered to decrease the stress around the cortical bone area.

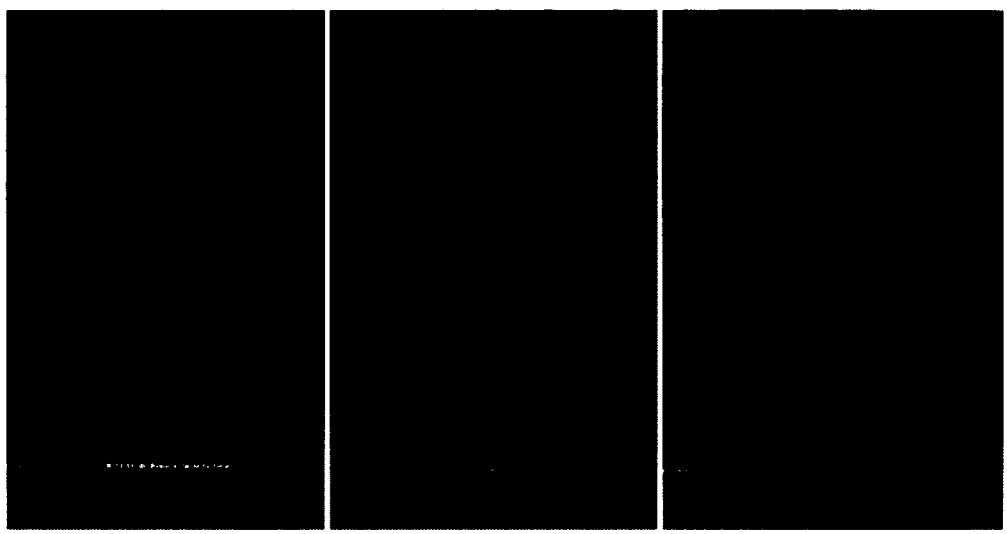

(a) σ_{ref} =1.14 MPa (b) σ_{ref} =1.15 MPa (c) σ_{ref} = 2.50MPa

Figure 6.15 Optimized Shape Under Different Reference Stresses With $k = 50$

Figure 6.15 provides the results under different loading conditions with fixed reference stress. Reference stress was picked up from Figure 6.15 (b) which has the most appropriate optimized implant shape considering the depth and width. Based on that, five different loads from 100 N to 250 N were applied to see how these loading conditions affect the structure. As seen from Figure 6.16 (a) – (d), significant difference exists between the loads. Thus, one should employ the different reference stress for each of the loading conditions. For the 2D case, axial load more than 250N will saturate the implant material through the cancellous bone area.

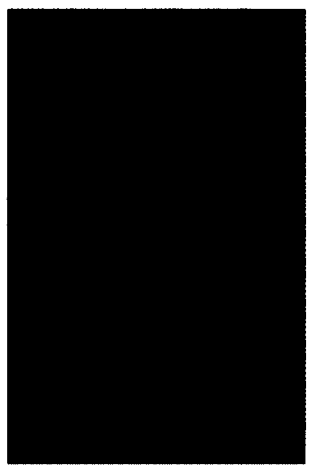

(a) $k = 50$, σ_{ref} =1.2MPa, F = 100N

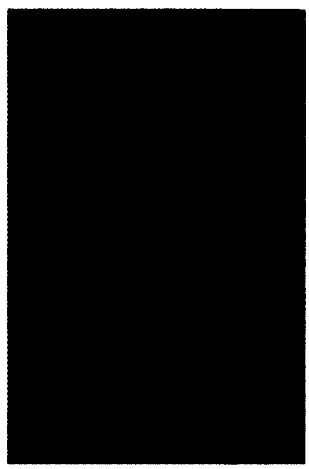

(b) $k = 50$, σ_{ref} =1.2MPa, F = 150N

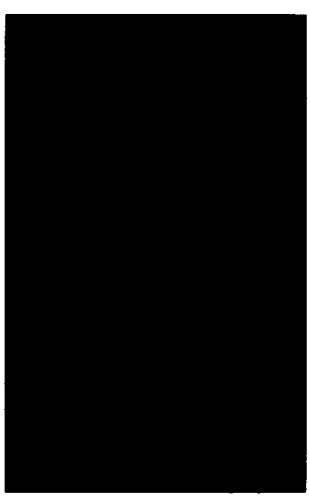

(c) $k = 50$, σ_{ref} =1.2MPa , F = 200N

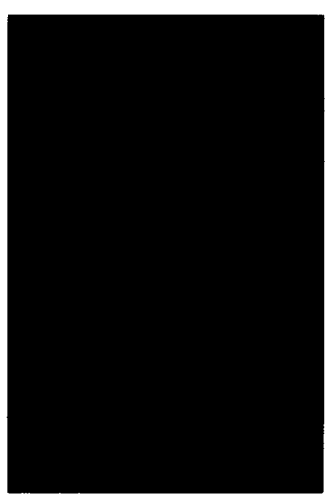

(d) $k = 50$, σ_{ref} =1.2MPa, F = 250N

Figure 6.16 Different Loading Under Fixed Reference Stress With $k = 50$

6.5.2 Modified Design

A modified model with the specimen insertion into cortical bone (see Figure 6.17) was created to determine whether specimen insertion can provide the possibility to

perform the SKO optimization for a 3D natural tooth-shaped root. Loading and boundary conditions are the same as in the initial design. Compared to the results of the previous section, the modified model has almost the same pattern of biological growth of the specimen in the cancellous bone area (see Figures 6.18 – 6.19). Residual stresses remain on the top of the cortical bone in Figures 6.18 (a) – (c) under certain reference stress.

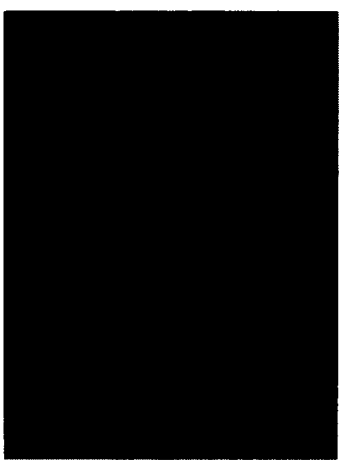

Figure 6.17 Modified Design Domain

In this dissertation, however, only the cancellous bone area plays a significant role as design space due to material properties.

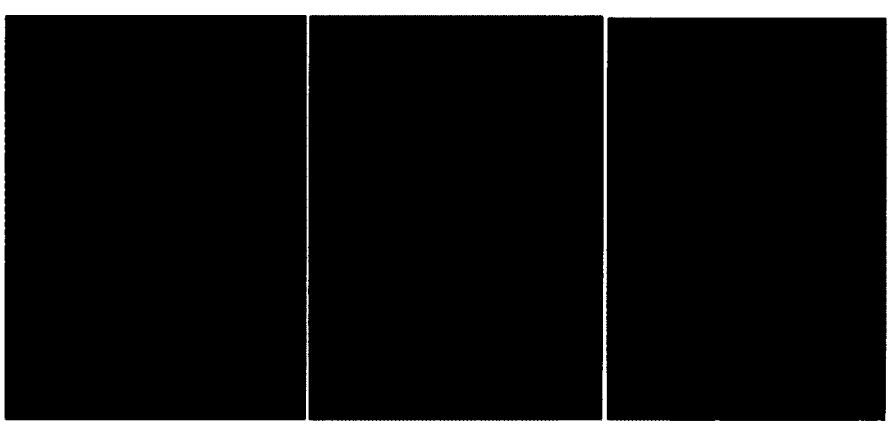

(a) k=50, σ_{ref} = 1.15MPa (b) k=50, σ_{ref} = 1.18MPa (c) k=50, σ_{ref} = 1.25MPa

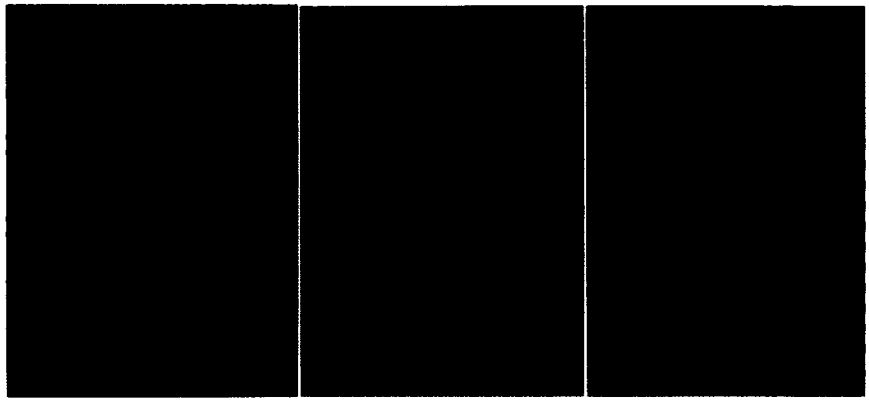

(d) k=50, σ_{ref} = 1.80MPa (e) k=50, σ_{ref} = 2.0MPa (f) k=50, σ_{ref} = 2.50MPa

Figure 6.18 Optimized Shapes Under Different Reference Stresses

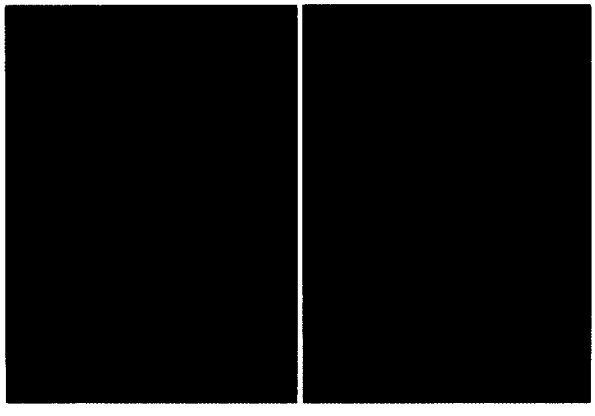

(a) k=50, F= 100N (b) k=50, F= 150N

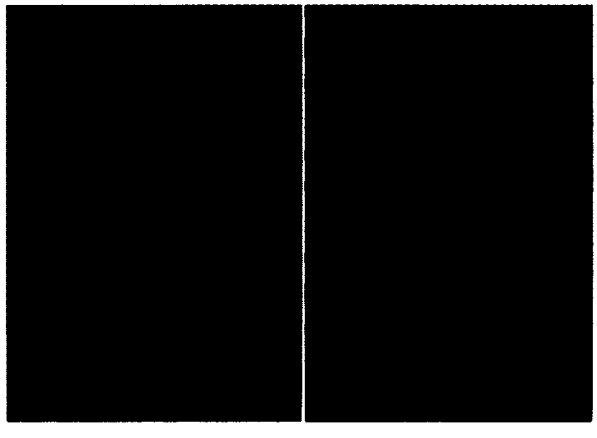

(c) K=50, F= 200N (d) k=50, F= 250N

Figure 6. 19 Different Loading Under Fixed Reference Stress, σ_{ref} = 1.2 MPa

6.6 Simulation Results – 3D FEA Model

6.6.1 Model Preparation

In this dissertation, two different types of natural root-shape CAD models were prepared for the Finite Element Analysis (FEA). Our standardized set of natural-root-form implants were designed based on the 3D shape of human teeth. The 3D models of human teeth were extracted from a digital, anatomically correct female skeleton. Among all the 32 teeth, the one-root part of tooth #29 and two-root part of tooth #30 were selected as the templates for FEA and further optimization since they are good representations of typical roots (see Figures 6.20 – 6.21).

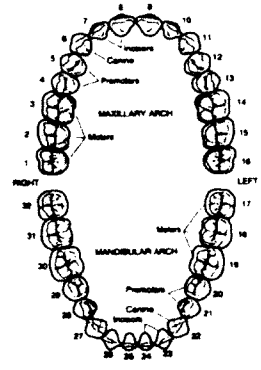

Figure 6.20 Numbering and Types of Human Teeth [62]

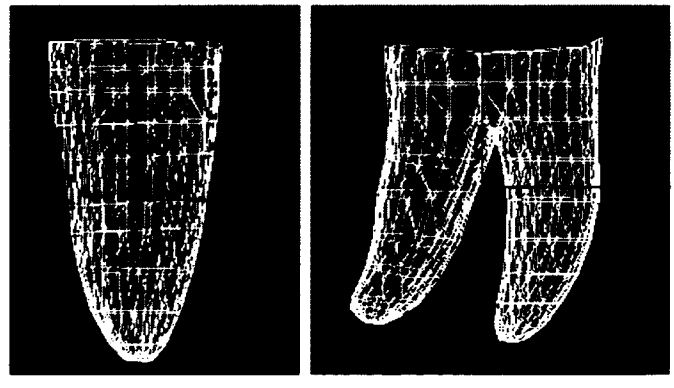

(a) One-root template (b) Two-root template

Figure 6.21 Templates of Natural-Root Shapes for FEA

After picking the templates for natural-root-form implants, shape refinement was required for the design. The shape of a natural root is obviously much more complicated than conventional cylinder-shaped implants. Robotic operation allows precise site preparation for the complex shapes of the natural-root-form that is not manually possible. However, due to the facts of the small scale and limited space available intra-orally, there is a need for simplification of the natural root shapes to make automated robotic milling of the implant site.

The biggest issues for natural-root-shape milling are the existence of sharp curvatures and undercuts. Therefore, two strategies were applied using Autodesk 3DS Max (Autodesk, Inc., CA) to get the refined shapes of the implants. First, we performed curvature smoothing since the root of a natural tooth tends to curve at its apex, as shown in Figure 6.22. While it might provide for better anchoring for the tooth, it requires frequent direction changes and undercuts for the milling tool, which may cause heating, failure, and obstructions during site preparation. We smoothed the curvature by creating a segmented system for each root along its central line and then adjusted the orientations of the segments or bones to make their connections smoother (see Figure 6.22(b)). The bones were generated according to the curvature of the original model. The conjunction between two adjacent bones lies in wherever larger curvature change occurs. We developed a simple script which reorients the position of the lower bone with respect to the upper bone, hence reducing curvature of the implant (see Figure 6.22 (c)). Similarly, curvature soothing was also applied to the template for other implant types.

(a) Initial template with bones (b) Smoothed template (c) Implant modeler windows

Figure 6.22 Curvature Smoothing

When the surface of the roots was carefully inspected after curvature smoothing, we found that there were still several undercuts in the models. Because the intraoral operation space is very small, no undercut can be manufactured in the jawbone. We applied an algorithm in Autodesk 3ds Max that accesses the position of three consecutive vertices along the centerline of the implant starting from an arbitrary point which typically is the vertex at the opening. If the position of the middle vertex is not approximately half of the distance, taking into account an arbitrary threshold, between the upper and the lower vertex, the position on the middle vertex was adjusted (see Figure 6.23).

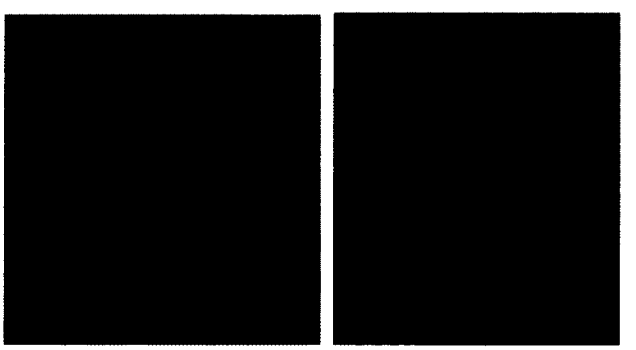

a) Model of the implant with undercuts b) Model of the implant with undercuts removed

Figure 6.23 Undercuts Removal

Through these procedures, *.obj files have been created to fill the holes of the given surface models in Figure 6.24. Solidworks 2010 was used to create the solid models based on root types.

(a) Anatomically correct models - One-Root

(b) Refined models – One-Root

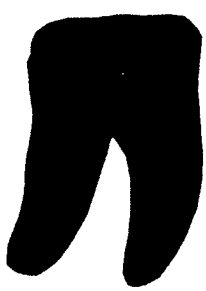

(c) Anatomically correct models – Two-Root

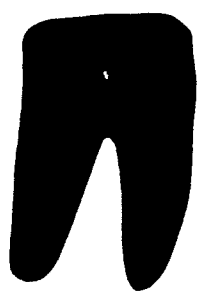

(d) Refined models – Two-Root

Figure 6.24 Two Types of Teeth in terms of the Tooth Shapes

Since a CAD based model is initially used in this study, the boundary shape is represented by NURBS curves and surfaces to control the curvature and tangency of the model [52]. Several papers described that during the optimization process, corners in the surfaces may become sharper, which increases the stresses in that region and can cause element distortion. In order to avoid numerical errors in the meshing and Jacobian calculations, sharp edges should be smoothed. Figure 6.25 shows the initial root-shape

implants of an anatomically correct model without crowns (a) and (b), while models in Figure 6.26 represent the robotic milling refined implants from Figure 6.25.

For the finite element analysis, models of Figures 6.25 – 6.26, anatomically correct models were filled, and the top surface was closed. Since original models have sharpness through the NURBS curves and surfaces, element size was reduced by 20%, and the surface was smoothed by 20% to avoid element distortion during finite element computation.

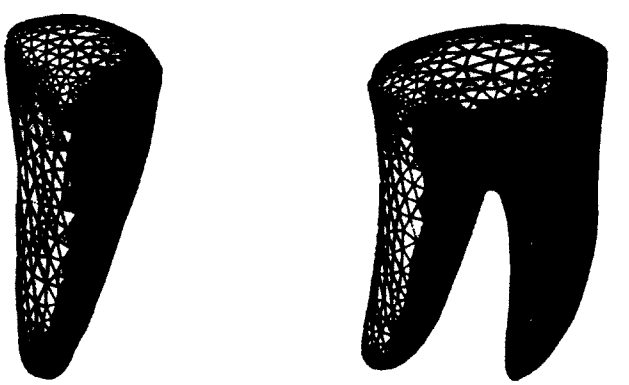

(a) One-root implant (b) Two-root implant

Figure 6.25 Anatomically Correct Models

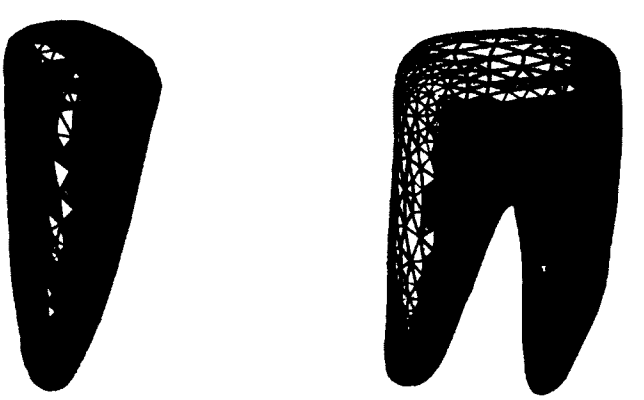

(a) One-root implant (b) Two-root implant

Figure 6.26 Refined Models

6.6.2 Finite Element Model

Two 3D finite element models were developed using the results of the CAD refinement that represent a segment of the human mandible with four natural teeth as implants. The model was constructed from the geometry identified in the previous section and processed in Rhinoceros 3.0 and Solidworks 2010. The finite element mesh was generated in 10-node quadratic tetrahedral elements using MSC PATRAN 2010, comprised of 30,217 elements for the one root implant and 98,494 elements for the two root implant after convergence (see Table 6.2). As shown in Figure 6.27, the model consists of three parts: cancellous bone, cortical bone, and the natural root-shaped implants. The material properties (see Table 6.3) of the implant and the bones are obtained from [50]. The interface between the cancellous and cortical bones and the implant root and the bones is assumed to be perfectly bonded. All materials used in this model are considered to be isotropic, homogeneous, and linearly elastic. Table 6.3 shows the elastic properties in terms of material types. The properties are the same in all directions; therefore, only two independent material constants of Young's modulus and Poisson's ratio exist in an isotropic material. In Figure 6.27, cancellous bone is surrounded by 1 mm thick cortical bone.

The boundary condition is applied along the bottom surface of the cortical bone and all around the sides to restrict translational and rotational movements of the structure. A load of 200 N in the vertical (z) direction was applied on the top surface of the implant, simulating a chewing force applied by the teeth from the maxillary side. The relationship between the force and angle changes with different teeth from different patients. Thus, in this research, only a vertical force was considered to simplify the process.

Table 6.2 Finite Element Configuration for the Anatomically Correct Models

Tooth Type	Elements	Nodes	Element Type
One-Root	30217	44088	C3D10
Two-Root	98494	136795	C3D10

Table 6.3 Material Properties for the Anatomically Correct Models

Materials	Young's Modulus (GPa)	Poisson's Ratio
Cortical Bone	13.7	0.3
Cancellous Bone	1.37	0.3
Implant(titanium)	110	0.33

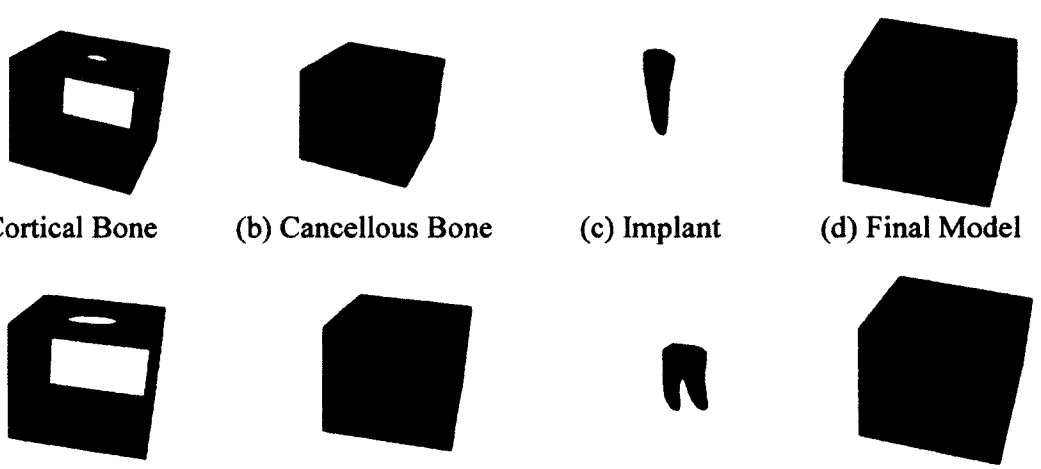

(a) Cortical Bone (b) Cancellous Bone (c) Implant (d) Final Model

(e) Cortical Bone (f) Cancellous Bone (g) Implant (h) Final Model

Figure 6.27 3D Dental Implants for One-Root and Two-Root Implants of An Anatomically Correct Model

6.6.3 Finite Element Results

The von Mises stress distribution was used to display the stress around the cortical and cancellous bone area. Stress distribution depends on assumptions made in geometry, material properties, boundary conditions, and bone-implant interface. Contour plots of von Mises stresses, recorded at the location of implant-bone contact, under axial load of 200N are shown along the insertion depth in Figures 6.28 (a) through (d). Through the half-cut of the model, nodal paths were generated to investigate how the stress varies through these lines for the one-root and two-root implants. Figure 6.29 illustrates that along the cortical and implant interface, a high level of von Mises stress with a maximum stress of 19.33 MPa for one-root and 17.9 MPa for two-root implants exists near the bone around the implant neck. The magnitude of stresses then decrease along the path and the increased stresses were shown around the implant root apex regions (Figures 6.28 (b) and (d) and Figures 6.29 (b) and (d)) in both the initial anatomically correct case and the refined case. However, the two-root implant has less von Mises stress distribution around the root apex areas than the one-root implants.

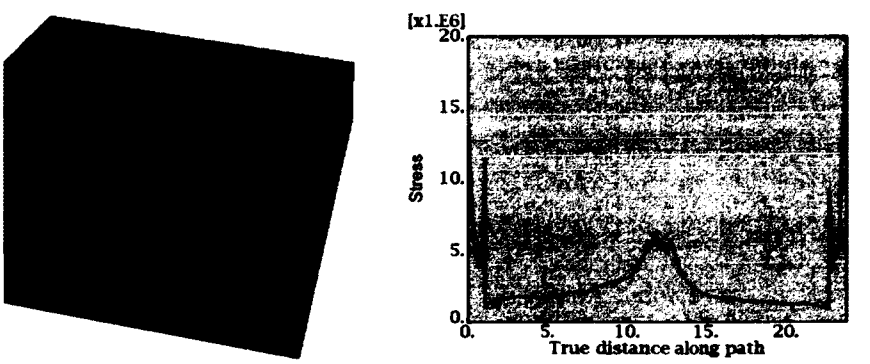

(a) Contour plots with nodal path (b) Von Mises stress levels along the nodal path

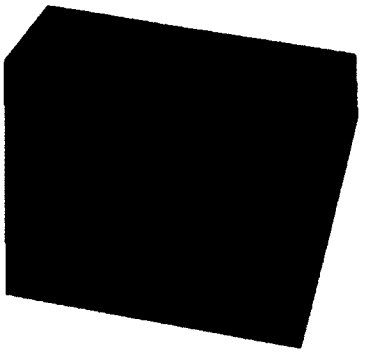

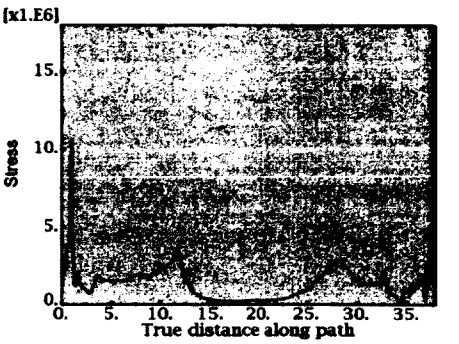

(c) Contour plots with nodal path (d) Von Mises stress levels along the nodal path

Figure 6.28 Stress Contours of the Anatomically Correct Models with One-Root and Two-Root Implants

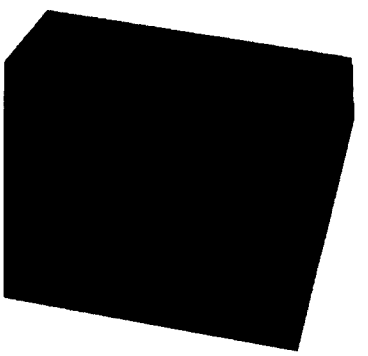

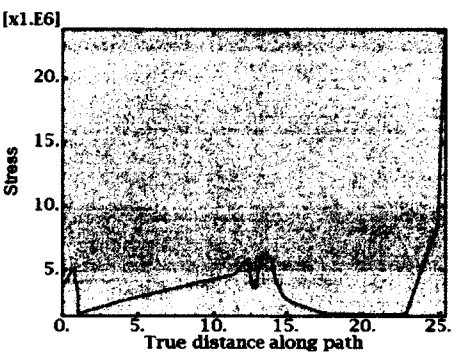

(a) Contour plots with nodal path (b) Von Mises stress levels along the nodal path

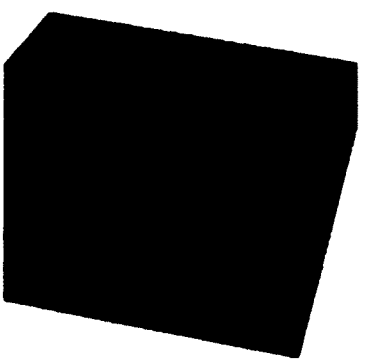

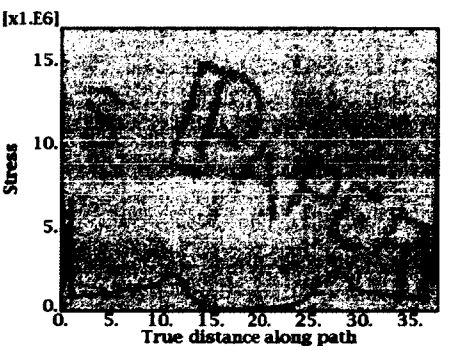

(c) Contour plots with nodal path (d) Von Mises stress levels along the nodal path

Figure 6.29 Stress Contours of the Robotic Milling Refined Models With One-Root and Two-Root Implants

6.6.4 SKO Results – Anatomically Correct and Refined Models

This section presents the results of SKO optimization of the anatomically correct and refined models. The results confirm a possibility that computer aided optimization may inspire understanding and modeling of complex natural root-shape implants. Through the optimization procedure, the geometric design space is specified, spanned with a finite element mesh and geometric boundary conditions as well as forces specified. Three Young's moduli are initially assigned to the two types of bone and the implant material of the finite elements in the design space. A structural analysis gives an initial solution to obtain a stress distribution over the domain. The stresses are combined to establish the distribution of an equivalent stress, which is the von Mises stress. The local optimality criterion used by Mattheck assumes that the stiffness of the design will globally increase when the Young's modulus is increased in regions with higher stresses and reduced where the stresses are lower. When the stresses fall below a certain threshold, the Young's modulus is replaced by the Young's modulus of cancellous or cortical bones. This serves to modulate the shape of the implant so that the optimal shape can be determined by the optimal distribution of stresses reflected in the changing Young's modulus regions.

The SKO optimization procedure yields the results plotted in Figures 6.30 – 6.33. In Figure 6.30, for example, reference stresses from 2 MPa to 4 MPa were used under the axial loading of 200N to see how the material property varies for one root implant of the anatomically correct model. Note that the gray and red color of the model has the same material property which is titanium. Optimized geometry adjacent to the original implant decreases progressively in thickness while increasing the reference stress. That means the

circumferential stress also decreases with increasing reference stress, but its maximum value is much lower than in the initial configuration. The thickness of the optimized implant model decreases progressively but at a slow rate with increasing distance to the root. The difference between the results shown in Figure 6.30 and Figure 6.31 is in the choice of the reference stress used for the optimization, since different stress magnitudes exist based on the root-shapes. In Figures 6.32 – 6.33, the refined model has a tendency to have more material property change in a low reference stress due probably to the wider geometric configuration than the one for the anatomically correct model.

Based on the optimized results, updated material of the top cortical bone area could be neglected since it has only 1 *mm* of thickness and our interest is focused near implant roots around the cancellous bone. Thus, it may be concluded that local details of the new implant shape depend on the choice of reference stress for the objective function while global features remain the same. Also, results illustrate that in order to reduce the stresses around the apex of roots, root-shapes should be more rounded. Such rounded root-shapes will be introduced in section 6.7.

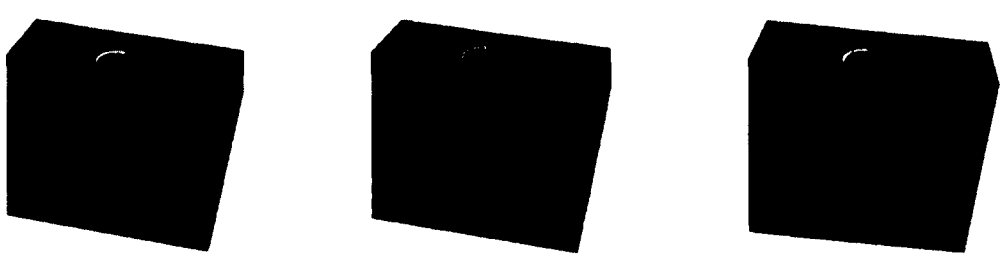

(a) σ_{ref} =2.0MPa, F=200N (b) σ_{ref} =3.0MPa, F=200N (c) σ_{ref} =4.0MPa, F=200N

Figure 6.30 Optimized Material Property for the One-Root Implant of An Anatomically Correct Model

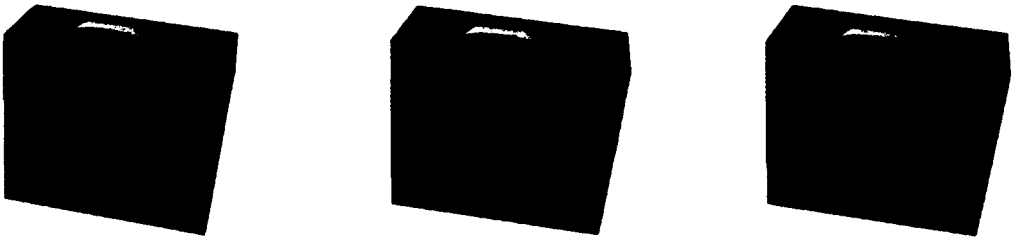

(a) σ_{ref} =1.65MPa, F=200N (b) σ_{ref} =1.8MPa, F=200N (c) σ_{ref} =2.2MPa, F=200N

Figure 6.31 Optimized Material Property for the Two-Root Implant of An Anatomically Correct Model

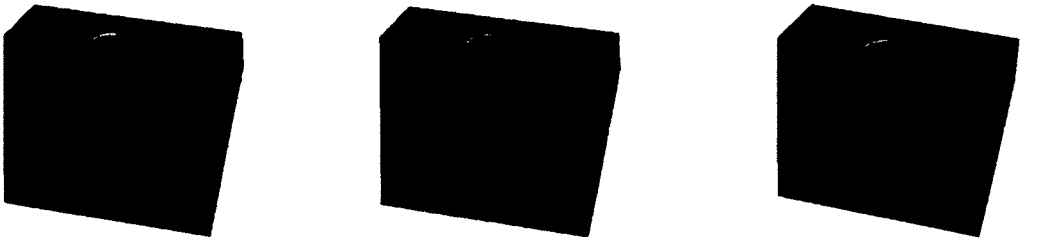

(a) σ_{ref} =2.0MPa, F=200N (b) σ_{ref} =3.0MPa, F=200N (c) σ_{ref} =4.0MPa, F=200N

Figure 6.32 Optimized Material Property for the One-Root Implant of A Refined Model

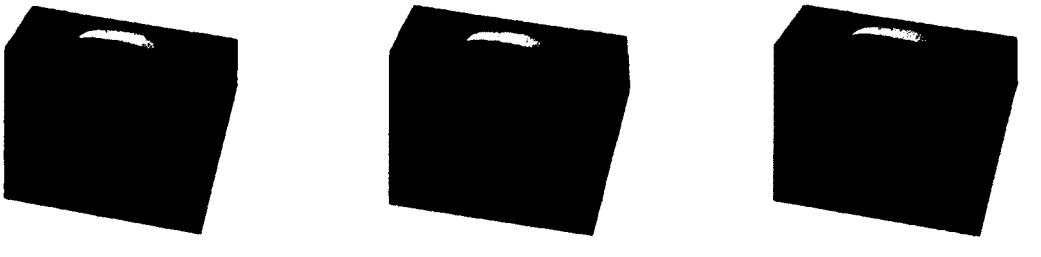

(a) σ_{ref} =1.65MPa, F=200N (b) σ_{ref} =1.8MPa, F=200N (c) σ_{ref} =2.2MPa, F=200N

Figure 6.33 Optimized Material Property for the Two-Root Implant of A Refined Model

6.7 Optimized Implants and FEA Results

Based on SKO results, new implant shapes are created. The new optimized models without crowns have more rounded shapes around the root-tips than the previous refined models (see Figures 6.34 (c) and (d)). FEM results of the optimized implants under an axial load of 200 N are shown in Figure 6.35. Table 6.4 shows the stress levels for the anatomically-correct models, robotic-milling-refined models and SKO-optimized models. First, for the one-root case, the optimized model with respect to the anatomically correct model reduced the maximum stress near the implant root-tip by 21.16% from 6.38 MPa to 5.03 MPa, while it was reduced by 39.01% for the two-root case. Additionally, comparing with respect to the robotic milling refined model, one-root and two-root implants have a stress reduction of 19.65% and 9.39%, respectively. Thus, the optimized implant model has significant stress decreases from both the anatomically correct model and the refined model. Figure 6.36, for example, shows the printed out designed models for the one-root and two-root implants.

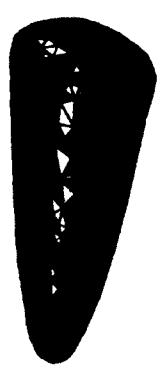

(a) One-root refined implant

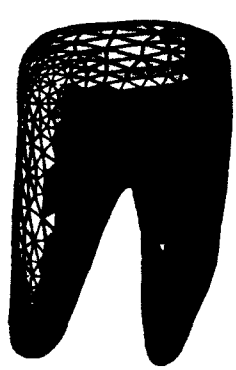

(b) Two-root refined implant

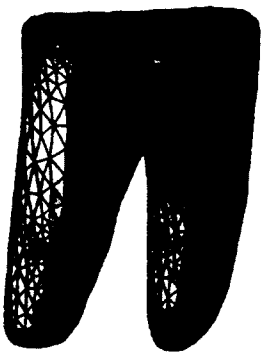

(c) One-root SKO optimized implant (d) Two-root SKO optimized implant

Figure 6.34 Implants with Refined and SKO Optimized Models

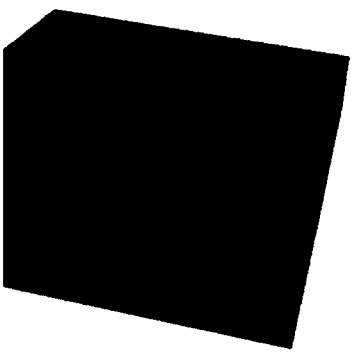

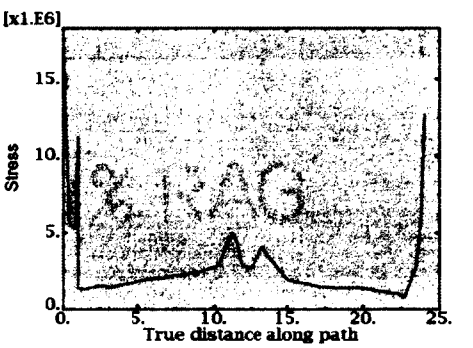

(a) Contour plots with nodal path (b) Von Mises stress levels along the nodal path

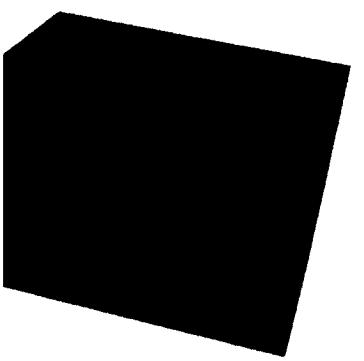

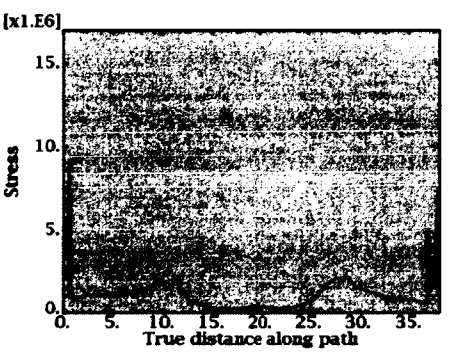

(c) Contour plots with nodal path (d) Von Mises stress levels along the nodal path

Figure 6.35 Stress Contours of the Optimized One-Root and Two-Root Implants

Table 6.4 Stress Levels of Three Different Types of Models

	Anatomically Correct Model (MPa)	Robotic Milling Refined Model (MPa)	Optimized Model		
			Value	% Change from Anatomically Correct Model	% Change from Refined Model
Max. One-Root	6.38	6.26	5.03	21.16	19.65
Max. Two-Root	3.64	2.45	2.22	39.01	9.39

Figure 6.36 Designed Models of One-Root and Two-Root Implants **[41]**

CHAPTER 7

EXPERIMENT RESULTS

In this chapter, phantom experimental results of a robotic milling system for acquisition of dental implants are focused on. Geometric volumes of the one-root and two-root implants were generated by Xiaoyan Sun from the Department of Electrical and Computer Engineering at Old Dominion University. Experiments were carried out using data points of the milling sequence with or without the sub-function defined by elliptical frustum in Figure 7.1. Geometrical parameters with volume sizes are summarized in Tables 7.1 – 7.2.

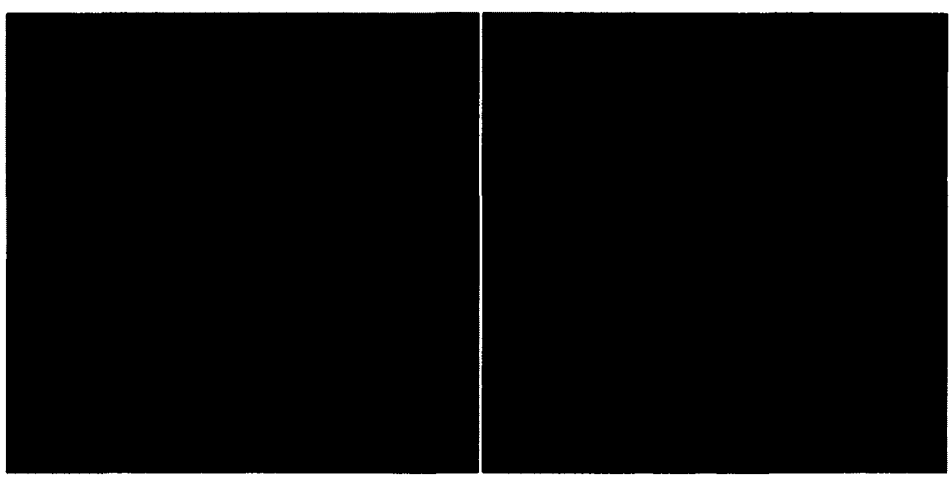

Figure 7.1 Point-Cloud Sets of Milling Sequence for One-Root and Two-Root Implants

Table 7.1 Parameters for the Robotic Milling Sequence of One-Root Implant

	With Elliptic Cone	Without Elliptic Cone
Drilling Direction	0.0099, 0.0297, -0.9995	0.0003, 0.0395, -0.9992
Starting Point	-0.0168, -0.1914, 5.3600	-
Ending Point	0.0769, 0.0908, -4.1400	-
Depth	9.50	-
Top Long Radius	2.1457	-
Top Short Radius	1.1143	-
Bottom Long Radius	1.0435	-
Bottom Short Radius	0.5419	-
Tilted Angle	34.3713	-
Number of Milling Sequential Points	91	1121

Table 7.2 Parameters for the Robotic Milling Sequence of Two-Root Implant

	Parameter	Top	Root I	Root II
With Elliptic Frustum	Drilling Direction	0.0000, 0.0000, -1.0000	-0.0872, 0.0527, -0.9948	-0.1033, 0.1602, -0.9817
	Starting Point	0.5969, -0.2504, 6.3200	0.7228, -2.3854, 2.7200	-0.0418, 1.6834, 2.7200
	Ending Point	0.5969, -0.2504, 4.3200	0.1532, -2.0412, -3.7800	-0.5682, 2.4991, -2.2800
	Depth	2	6.5340	5.0934
	Top Long Radius	3.3145	2.2326	2.4208
	Top Short Radius	3.0017	0.7792	0.8953
	Bottom Long Radius	2.8342	1.0831	1.6396
	Bottom Short Radius	2.5667	0.3780	0.6064
	Tilted Angle	-38.4430	7.1892	0.6538
	Number of Milling Sequential Points	547	1	342
Without Elliptic Frustum	Drilling Direction	-0.0684, 0.0207, -0.9974	-0.0811, -0.0227, -0.9965	-0.1178, 0.1792, -0.9767
	Number of Milling Sequential Points	813	1391	1404

As seen in the above tables, four different types of volumes were implemented into the MELFA robot controller. Algorithms of sub-functions for the milling sequence of each type of implant shape were directly employed from Chapter 4. Results are given in Tables 7.3 – 7.4, while Tables 7.3 and 7.4 summarize the drilling times and data sizes for volume removal of the different implant shapes using a point cloud or subroutine milling

sequences. One can see that drilling duration using volume-decomposition from subroutines for one-root and two-root implants over the same robot override speed, v = 2 mm/s, is about 2.2 and 1.5 times shorter than the point cloud milling time, respectively. From the experiment, it can be concluded that volume dimension, data points of milling sequence, step size of robot path and robot movement speed affect the drilling time of volume removal.

Table 7.3 Comparison of Drilling Duration for Implant Types

Geometry Type		Parameter		Drilling Time (sec)	Data Size
One-Root	With Elliptic Frustum	V = 2 mm/s, r=3, h=9.50		177.01	91
	Without Elliptic Frustum	V = 2 mm/s		391.03	1121
Two-Root	With Elliptic Frustum	Top	V = 2 mm/s, r=3, h=2	941.35	1555
		Root I	V = 2 mm/s, r=3, h=5.61		
		Root II	V = 2 mm/s, r=3, h=6.52		
	Without Elliptic Frustum	Top	V = 2 mm/s	1465.7	3608
		Root I			
		Root II			

Table 7.4 Comparison of Drilling Duration for Combined Two-Root Implant

	Elliptic Frustum	Parameter	Drilling Time (sec)	Data Size
Top	Yes	V = 2 mm/s	231.09	1224
Root I	Yes	V = 2 mm/s	369.67	109
Root II	No	V = 2 mm/s	818.13	1391

Figures 7.2 – 7.5 show the graphical aspects of the volume removal using the above milling information. Through the figures, the step size of the volume removal for the height was increased by 0.5 mm. Especially in Figure 7.5, volume-decomposition for the two-root implant was composed of three elliptic-frustum, and each of them also included points set which had to be milled out at the bottom of the frustum.

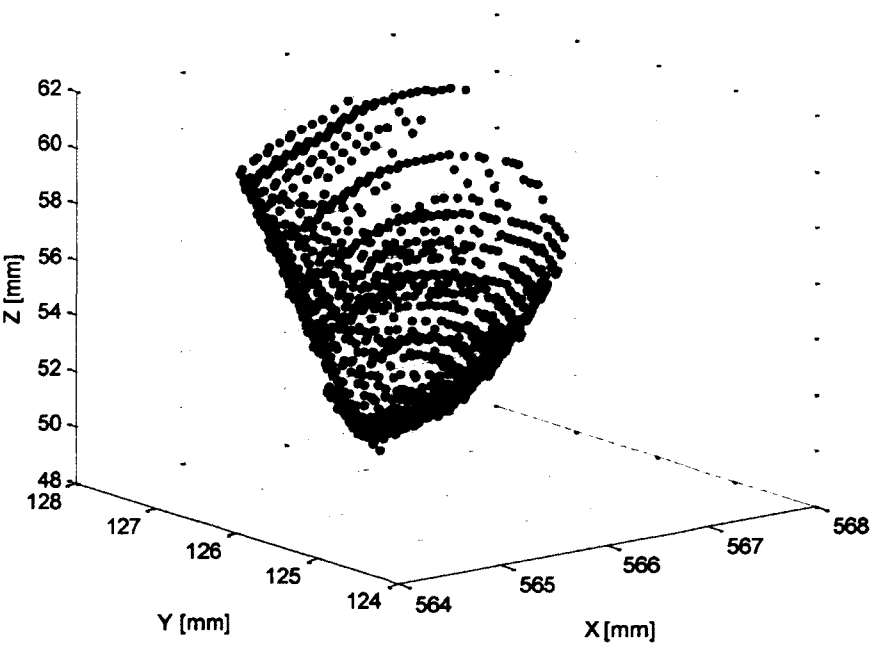

Figure 7.2 Point Cloud Milling Sequence for One-Root Implant

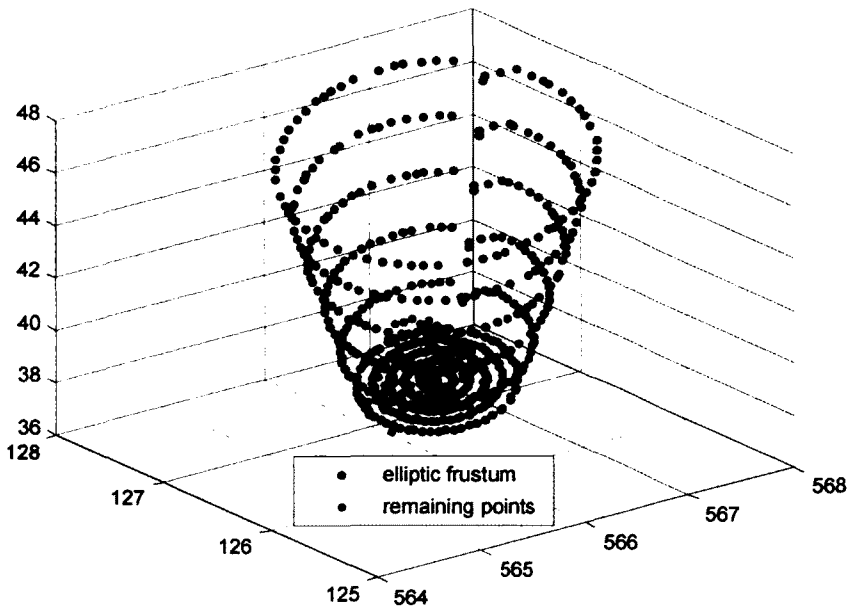

Figure 7.3 Volume-Decomposition Milling Sequence for One-Root Implant

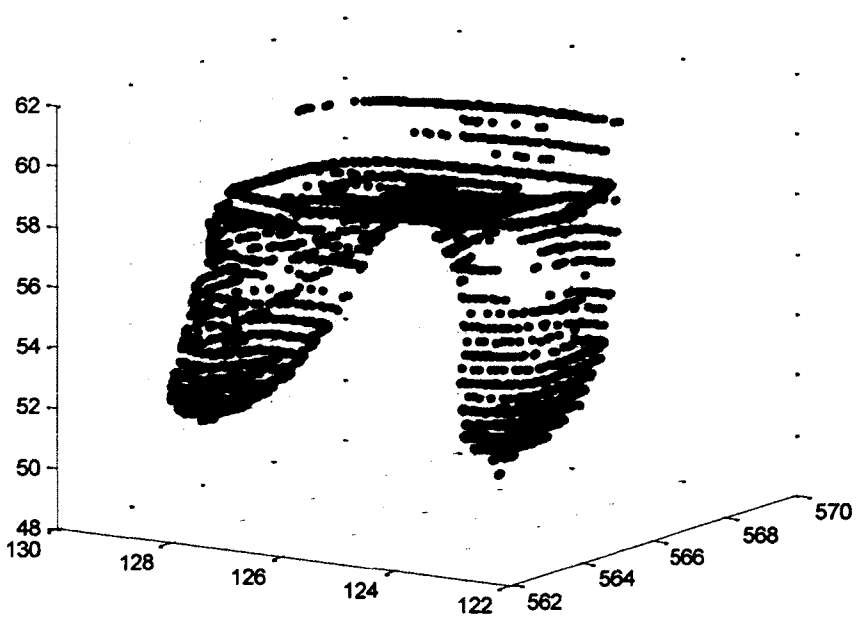

Figure 7.4 Point Cloud Milling Sequence for Two-Root Implant

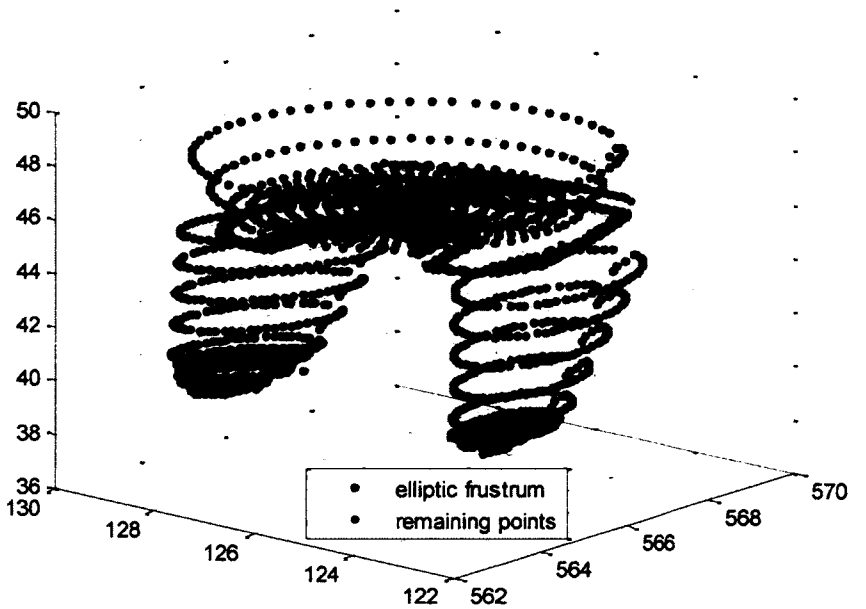

Figure 7.5 Volume-Decomposition Milling Sequence for Two-Root Implant

Figures 7.6 – 7.7 show the milling results for the one-root and two-root implants with respect to different types of milling sequence combination. Figure 7.6 also illustrates the overall view of all the combinations which were dealt with in the experiments. In Figure 7.7, several trials were carried out to find the right shape as proposed in Figure 7.7(a). Figure 7.7(b1) uses a volume-decomposition algorithm which had a regional violation on the right bottom area indicated by the red rectangular box. This is due to the orientation angle setup of the drill-bit (see Table7.2) and unwanted deviations from the drill-bit during the milling process. The deviations arise from the vibrations of the drill-bit during drilling. The actual radius of the drill-bit is 1 *mm*; however, an averaged deviation of approximately 0.25 *mm* occurs during the process. From Figures 7.7 (b1) and (b2), a

point cloud sequence had less deviation in the downward direction, but increases are shown in width. The contour line at the top compared to the original shape in (a) is less defined at the edge, while (b1) had more tendency to follow the contour. To fix these issues the combination of the volume-decomposition and point cloud sequences was applied. Figure 7.7 (b3) contains the characteristics for both algorithms but still has the undesired removal on the right bottom area. FEM results from Chapter 6 showed that von Mises stress distribution around a root portion was significantly less than the interface between the cortical bone and implants. Therefore, in Figure 7.7 (b4), we straightened the right root to avoid violating the undesired contour by considering the orientation of the drill-bit. The drill-bit set vertical down and volume-decomposition algorithm was used as (b1). Comparing all the figures, Figure (b4) has a smoother contour line on the top surface as well as having shorter milling time than the point cloud method, while almost avoiding violation of the designed contour at the bottom.

Figure 7.6 Milling Results for One-Root Implant: (a) Using Volume-Decomposition based Algorithm; (b) Using Point Cloud Sequence Milling

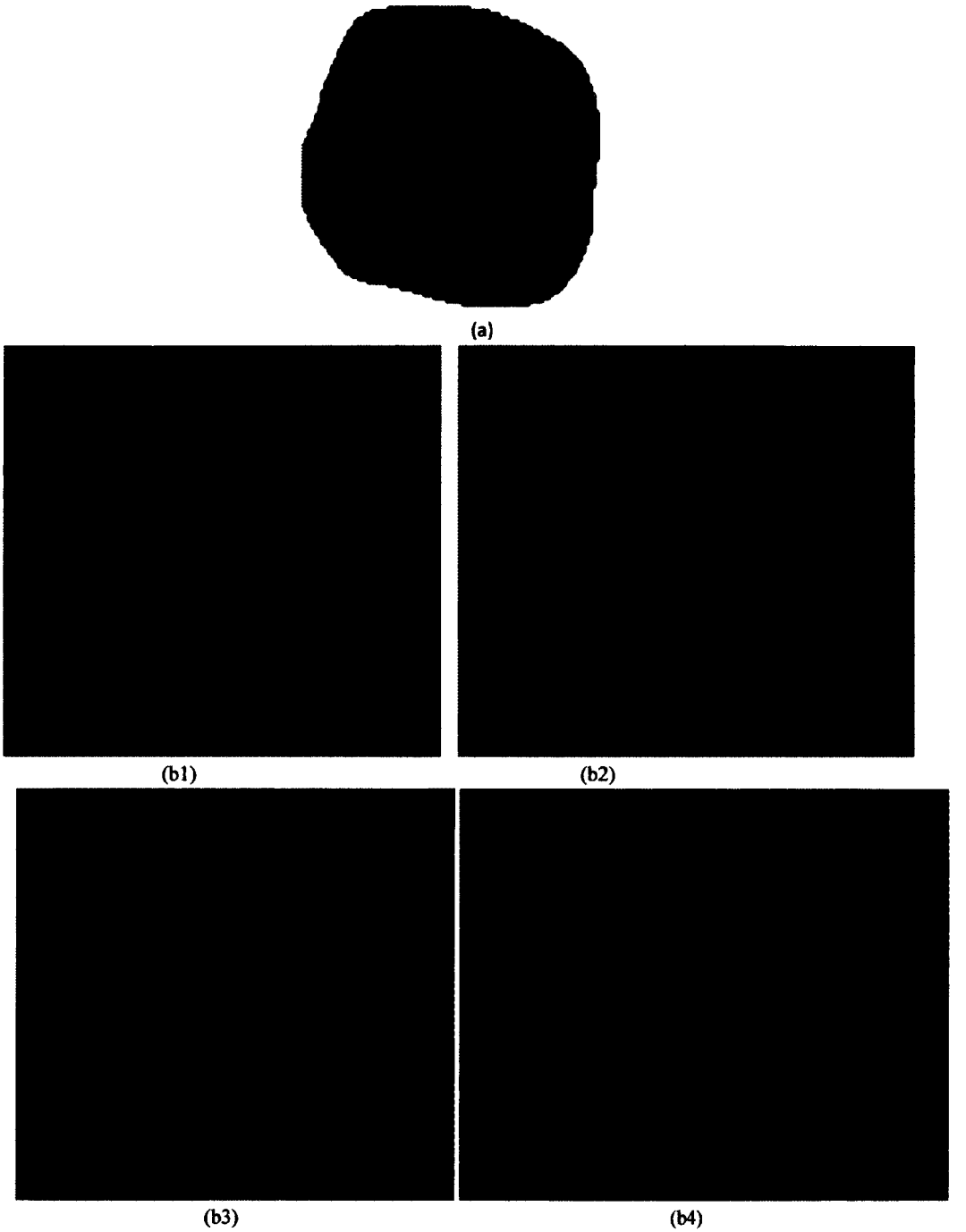

Figure 7.7 Milling Result for Two-Root Implant : (a) Top View of the Designed Two-Root Volume; (b1) Using Volume-Decomposition based Algorithm; (b2) Using Point Cloud Sequence Milling; (b3) Using a Combination of Volume-Decomposition and Point Cloud Sequence Milling; (b4) Using Volume-Decomposition with a Straightened Root [41]

Six holes of different volumes were filled carefully with dental material in Figure 7.8, while Figure 7.9 shows the extracted molds of the natural tooth-shaped models. Two times of molding processes were performed due to the break of the models (see first row in Figure 7.9). Molds from the first and second rows have the missing part at the root area since bulbs were contained during the filling process of dental material due to the small space at the bottom of the roots. Table 7.5 provides the dimensions of the molds. Note d_1 and d_2 denote the maximum and minimum length of the top surface, while l and l_s denotes the designed and measured heights of the molds, respectively. From the results, measured lengths and heights for the one-root and two-root implants are all inside of the designed boundary. During the drilling for volume removal, an air blower was used to clean up the power in the hole. However, due to the material characteristic of the plaster, it was easy to break the milled out holes during the cleaning process. This issue brought very careful treatment of the blowing stage and caused powder accumulation around the root tip space. Thus, compared to the length of the top surface, heights have high deviation.

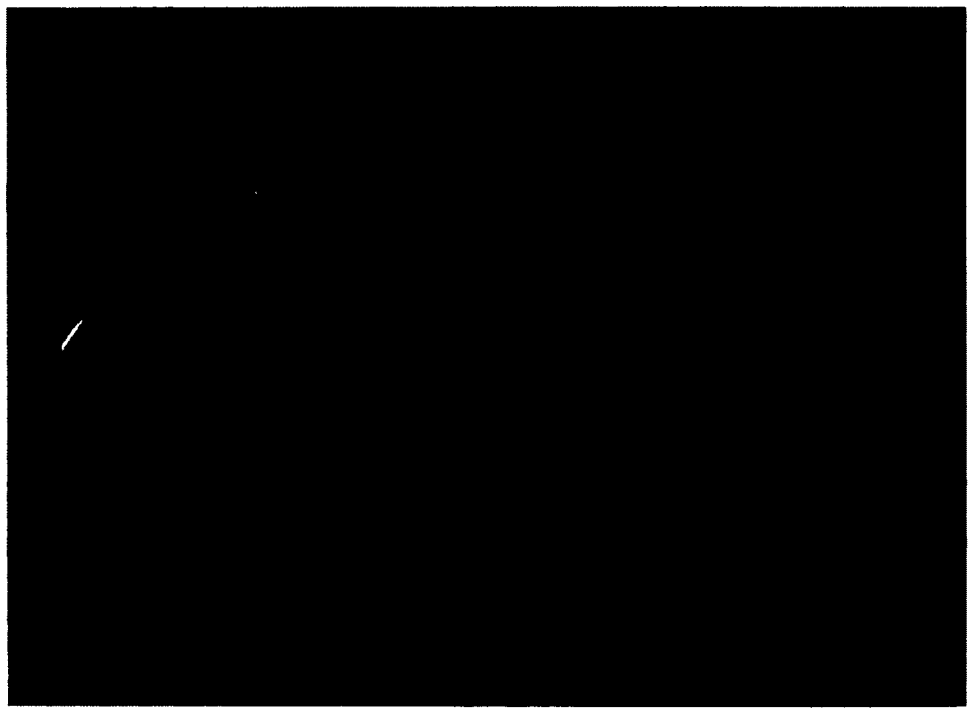

Figure 7.8 Molding the Milled Out Implant Holes

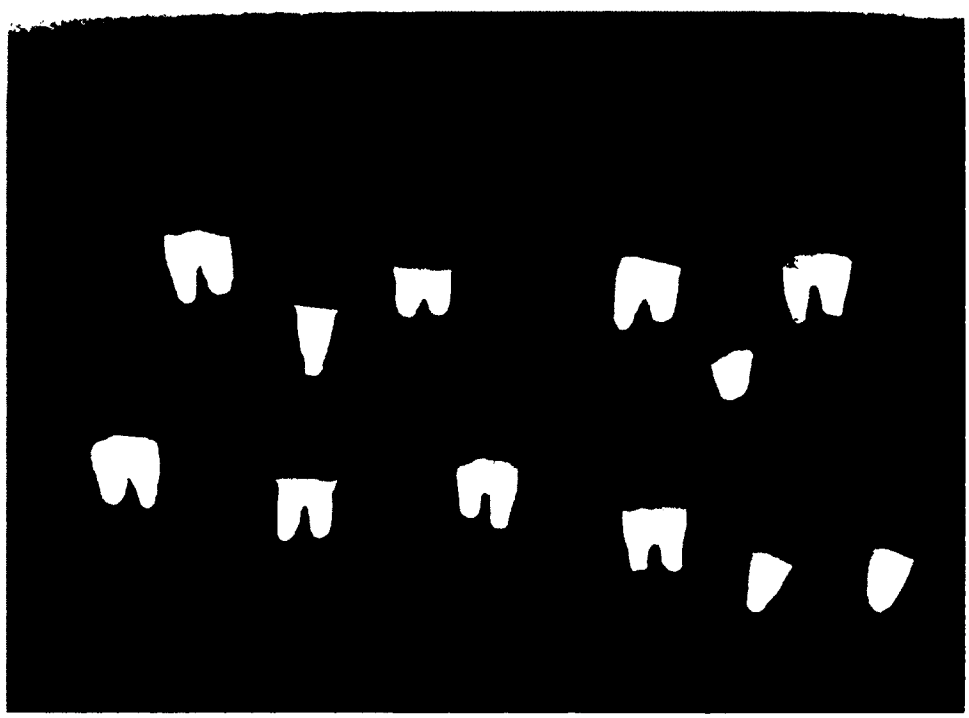

Figure 7.9 Molded Natural Tooth-Shaped Models via Different Milling Sequences

Table 7.5 Volume Dimension Between Designed and Molded Models

Types		d_1	d_2	l	l_s	l_1	L_{1s}	l_2	l_{2s}
S1	Designed	6.82	4.76	11.90	10.94				
	Measured	6.23	4.40	8.63					
	Error	-0.59	-0.36	-3.27	-2.31				
S2	Designed	6.82	4.58	11.84	11.28				
	Measured	6.43	4.43	9.40					
	Error	-0.39	-0.15	-2.44	-1.88				
D1	Designed	8.94	9.06			10.24	9.36	9.78	9.19
	Measured	9.78	8.70			9.71		9.25	
	Error	0.84	-0.35			-0.52	0.36	-0.53	0.06
D2	Designed	8.42	8.16			10.76	9.81	9.74	9.36
	Measured	8.97	8.53			9.35		8.72	
	Error	0.55	0.37			-1.42	-0.47	-1.03	-0.64
D3	Designed	8.94	9.06			10.76	9.81	9.78	9.19
	Measured	8.75	8.81			8.69		7.27	
	Error	-0.19	-0.24			-2.07	-1.12	-2.51	-1.92
D4	Designed	8.94	9.01			10.27	9.78	9.50	9.50
	Measured	9.44	8.02			9.97		9.60	
	Error	0.50	-0.99			-0.30	0.19	0.10	0.10
	Mean	0.51	0.41	2.85	2.10	1.08	0.53	1.04	0.68
	STD	0.58	0.44	0.59	0.31	0.82	0.67	1.11	0.95

Note S1: VD Sequence, S2: Point Clouse Sequence, D1: VD Sequence D2: Point Cloud Sequence, D3: Combined with VD and Point Cloud Sequences, D4: VD Sequence with a Straightened Root

CHAPTER 8

CONCLUSION

In this dissertation, a fully integrated robotic milling system was introduced to perform the automated dental implantation. For accurate implantation, preoperative planning of the patient's registration, using medical images and a coordinate measurement machine, and an intra-operative procedure using a six degrees of freedom robot arm were employed.

In preoperative planning, from a patient-specific model reconstructed using CBCT images, position and orientation of the implant were adjusted for insertion in the patient's jawbone. A two-step registration was used to transform the coordinate information of the patient to the robot operation. To provide accurate information between the robot and the patient coordinate systems, the coordinate measurement machine was used. Phantom experimental results provided that errors of the position and orientation after registration were 0.36 ± 0.13 *mm* and $1.99 \pm 1.27°$, respectively.

Two possible novel implants were studied for clinical use. In order to get the ideal natural tooth-shaped implants, refinement and SKO optimization techniques to design the natural root-shapes of dental implants were employed. The anatomically correct models and refined models were employed to study how the material properties vary and how the implant geometry can be optimized under boundary and loading conditions with certain constraints. The results of the finite element analysis and optimization proved that natural tooth-shaped implants provided less stress distribution than a conventional cylinder-shaped implant. Thus, the consideration of natural root-shaped implants allowed us to model the true biomechanical environment based on biological adaptive growth. Through

this procedure, optimized natural root-shaped implants were created for robot milling which was performed to prepare the root shape for the implant at the implant site.

In the intra-operative procedure, the robotic milling process was performed using a robot arm which has six degrees of freedom. Six different milling algorithms were implemented into the robot controller: cone, cylinder, elliptic cone, elliptic frustum, single-root and double-root implants. Based on the optimized implant shapes, two types of robotic milling sequence were applied for the implant types to compare the milling time and volume dimension. For the patient's safety, boundaries of the robot's workspace and joint's manipulation, and the drill-bit rotary speed were constrained during the milling process. In addition, vibration tests proved that the deviation of the drill-bit's position during spinning did not play an important role for the whole milling operation.

A point-cloud sequence only provided a set of discrete volume points, while implant models from volume-decomposition were segmented into the root and elliptic-frustum. Thus, drilling time and volume dimension comparison for both methodologies were evaluated regarding the combination of the sequences, especially in two-root implants. The results showed that the volume-decomposition sequence made the milling time shortened compared to the point-clouds method, and the removed volume kept the designed shape of the implant under boundary conditions.

In future research, it is necessary to investigate various surface preparation methodologies that will promote bone integration and encourage further stability of these implants. Additionally, proper manufacturing methods for such implants should be investigated.

REFERENCES

[1] D. Schwartz-Arad, N. Kidron, and E. Dolev, "A long-term study of implants supporting overdentures as a model for implant success," *Journal of Periodontology,* vol. 76, pp. 1431-1435, 2005.

[2] R. H. Taylor, "A perspective on medical robotics," *Proceedings of the IEEE,* vol. 94, pp. 1652-1664, 2006.

[3] R. C. Van Staden, H. Guan, and Y. C. Loo, "Application of the finite element method in dental implant research," *Computer Methods in Biomechanics and Biomedical Engineering,* vol. 9, pp. 257-270, 2006.

[4] Y. S. Kwoh, J. Hou, E. A. Jonckheere, and S. Hayati, "A robot with improved absolute positioning accuracy for CT guided stereotactic brain surgery," *Biomedical Engineering, IEEE Transactions on,* vol. 35, pp. 153-160, 1988.

[5] B. L. Davies, R. D. Hibberd, W. S. Ng, A. G. Timoney, and J. E. A. Wickham, "The development of a surgeon robot for prostatectomies," *ARCHIVE: Proceedings of the Institution of Mechanical Engineers, Part H: Journal of Engineering in Medicine 1989-1996 (vols 203-210),* vol. 205, pp. 35-38, 1991.

[6] H. A. Paul, W. L. Bargar, B. Mittlestadt, B. Musits, R. H. Taylor, P. Kazanzides, J. Zuhars, B. Williamson, and W. Hanson, "Development of a surgical robot for cementless total hip arthroplasty," *Clinical Orthopaedics and Related Research,* vol. 285, p. 57, 1992.

[7] L. Mettler, M. Ibrahim, and W. Jonat, "One year of experience working with the aid of a robotic assistant (the voice-controlled optic holder AESOP) in gynaecological endoscopic surgery," *Human Reproduction,* vol. 13, p. 2748, 1998.

[8] J. M. Sackier and Y. Wang, "Robotically assisted laparoscopic surgery," *Surgical Endoscopy,* vol. 8, pp. 63-66, 1994.

[9] J. Binder and W. Kramer, "Robotically-assisted laparoscopic radical prostatectomy," *BJU International,* vol. 87, pp. 408-410, 2001.

[10] P. I. Brånemark, U. Breine, R. Adell, B. O. Hansson, J. Lindström, and Å. Ohlsson, "Intra-osseous anchorage of dental prostheses: I. experimental studies,"

Scandinavian Journal of Plastic and Reconstructive Surgery and Hand Surgery, vol. 3, pp. 81-100, 1969.

[11] H. A. Hansson, T. Albrektsson, and P. I. Brånemark, "Structural aspects of the interface between tissue and titanium implants," *The Journal of Prosthetic Dentistry,* vol. 50, p. 108, 1983.

[12] D. R. Carter, "The relationship between in vivo strains and cortical bone remodeling," *Critical Reviews in Biomedical Engineering,* vol. 8, p. 1, 1982.

[13] D. R. Carter and G. S. Beaupré, *Skeletal function and form: mechanobiology of skeletal development, aging, and regeneration*: Cambridge Univ Pr, 2007.

[14] Y. Fung, *Biomechanics: motion, flow, stress, and growth*: Springer, 1990.

[15] J. D. Humphrey, *Cardiovascular solid mechanics: cells, tissues, and organs*: Springer Verlag, 2002.

[16] L. A. Taber, "Biomechanics of growth, remodeling, and morphogenesis," *Applied Mechanics Reviews,* vol. 48, p. 487, 1995.

[17] D. Lin, Q. Li, W. Li, N. Duckmanton, and M. Swain, "Mandibular bone remodeling induced by dental implant," *Journal of Biomechanics,* vol. 43, pp. 287-293, 2010.

[18] R. Huiskes, M. Dalstra, R. vd Venne, H. Grootenboer, and T. J. Slooff, "A hypothesis concerning the effect of implant rigidity on adaptive cortical bone remodelling in the femur," Journal of Biomechanics, vol. 20, pp. 808-809, 1987.

[19] H. Weinans, R. Huiskes, and H. J. Grootenboer, "The behavior of adaptive bone-remodeling simulation models," *Journal of Biomechanics,* vol. 25, pp. 1425-1441, 1992.

[20] S. D. Cook, A. L. Weinstein, and J. J. Klawitter, "A Three-Dimensional Finite Element Analysis of a Porous Rooted Co-Cr-Mo Alloy Dental Implant," *J Dent Res,* pp. 61:25-9, 1982.

[21] R. Skalak, "Biomechanical considerations in osseointegrated prostheses," *The Journal of Prosthetic Dentistry,* vol. 49, p. 843, 1983.

[22] C. S. Petrie and J. L. Williams, "Comparative evaluation of implant designs: influence of diameter, length, and taper on strains in the alveolar crest," *Clinical Oral Implants Research,* vol. 16, pp. 486-494, 2005.

[23] M. R. Rieger, M. Mayberry, and M. O. Brose, "Finite element analysis of six endosseous implants," *The Journal of Prosthetic Dentistry,* vol. 63, pp. 671-676, 1990.

[24] Y. Akagawa, Y. Sato, E. R. Teixeira, N. Shindoi, and M. Wadamoto, "A mimic osseointegrated implant model for three-dimensional finite element analysis," *Journal of Oral Rehabilitation,* vol. 30, pp. 41-45, 2003.

[25] S. Tada, R. Stegaroiu, E. Kitamura, O. Miyakawa, and H. Kusakari, "Influence of implant design and bone quality on stress/strain distribution in bone around implants: a 3-dimensional finite element analysis," *The International Journal of Oral & Maxillofacial Implants,* vol. 18, p. 357, 2003.

[26] C. S. Petrie and J. L. Williams, "Shape optimization of dental implant designs under oblique loading using the p-version finite element method," *Journal of Prosthodontics,* vol. 11, pp. 333-334, 2002.

[27] H. S. Hedia and N. A. Mahmoud, "Design optimization of functionally graded dental implant," *Biomedical Materials and Engineering,* vol. 14, pp. 133-144, 2004.

[28] J. M. García-Aznar, T. Rueberg, and M. Doblaré, "A bone remodelling model coupling microdamage growth and repair by 3D BMU-activity," *Biomechanics and Modeling in Mechanobiology,* vol. 4, pp. 147-167, 2005.

[29] T. Rüberg, "Computer simulation of adaptive bone remodeling," *Technische Universität Braunschweig, Centro Polictécnico Superior Zaragoza,* 2003.

[30] S. Adeeb and W. Herzog, "Simulation of biological growth," *Computer Methods in Biomechanics and Biomedical Engineering,* vol. 12, pp. 617-626, 2009.

[31] J. Duyck, I. Naert, H. J. Rønold, J. E. Ellingsen, H. Van Oosterwyck, and J. Vander Sloten, "The influence of static and dynamic loading on marginal bone reactions around osseointegrated implants: an animal experimental study," *Clinical Oral Implants Research,* vol. 12, pp. 207-218, 2001.

[32] F. Isidor, "Loss of osseointegration caused by occlusal load of oral implants. A clinical and radiographic study in monkeys," *Clinical Oral Implants Research,* vol. 7, pp. 143-152, 1996.

[33] G. Couegnat, S. L. Fok, J. E. Cooper, and A. J. E. Qualtrough, "Structural optimization of dental restorations using the principle of adaptive growth," *Dental Materials,* vol. 22, pp. 3-12, 2006.

[34] B. Davies, "A review of robotics in surgery," *Proceedings of the Institution of Mechanical Engineers, Part H: Journal of Engineering in Medicine,* vol. 214, p. 129, 2000.

[35] R. D. Howe and Y. Matsuoka, "Robotics for surgery," *Annual Review of Biomedical Engineering,* vol. 1, pp. 211-240, 1999.

[36] J. Brief, S. Haßfeld, R. Boesecke, M. Vogele, R. Krempien, M. Treiber, and J. Mühling, "Robot assisted Dental Implantology," *International Poster Journal,* vol. 4, 2002.

[37] P. Rhienmora, P. Haddawy, M. N. Dailey, P. Khanal, and S. Suebnukarn, "Development of a dental skills training simulator using virtual reality and haptic device," *NECTEC Technical Journal,* vol. 8, pp. 140-147, 2008.

[38] F. Watzinger, W. Birkfellner, F. Wanschitz, W. Millesi, C. Schopper, K. Sinko, K. Huber, H. Bergmann, and R. Ewers, "Positioning of dental implants using computer-aided navigation and an optical tracking system: case report and presentation of a new method," *Journal of Cranio-Maxillofacial Surgery,* vol. 27, pp. 77-81, 1999.

[39] D. X. Wang, Y. Zhang, Y. Wang, and P. Lu, "Development of dental training system with haptic display," *The 12th IEEE International Workshop on Robot and Human Interactive Communication,* pp. 159-164, 2003.

[40] X. Sun, F. D. McKenzie, S. Bawab, J. Li, Y. Yoon, and J. K. Huang, "Automated dental implantation using image-guided robotics: registration results," *International Journal of Computer Assisted Radiology and Surgery,* pp. 1-8, 2011.

[41] X. Sun, "Image-guided robotic dental implantation with natural root-formed implants," *PH.D Dissertation, Department of Electrical and Computer Engineering, Old Dominion University, Norfolk, Virginia,* May, 2012.

[42] W. Sun, A. Darling, B. Starly, and J. Nam, "Computer-aided tissue engineering: overview, scope and challenges," *Biotechnology and Applied Biochemistry,* vol. 39, pp. 29-47, 2004.

[43] E. P. Holmgren, R. J. Seckinger, L. M. Kilgren, and F. Mante, "Evaluating parameters of osseointegrated dental implants using finite element analysis—a two-dimensional comparative study examining the effects of implant diameter, implant shape, and load direction," *Journal of Oral Implantology,* vol. 24, pp. 80-88, 1998.

[44] T. W. P. Korioth and A. Versluis, "Modeling the mechanical behavior of the jaws and their related structures by finite element (FE) analysis," *Critical Reviews in Oral Biology & Medicine,* vol. 8, pp. 90-104, 1997.

[45] P. Ausiello, A. Apicella, C. L. Davidson, and S. Rengo, "3D-finite element analyses of cusp movements in a human upper premolar, restored with adhesive resin-based composites," *Journal of Biomechanics,* vol. 34, pp. 1269-1277, 2001.

[46] P. Ausiello, A. Apicella, and C. L. Davidson, "Effect of adhesive layer properties on stress distribution in composite restorations--a 3D finite element analysis," *Dental Materials,* vol. 18, pp. 295-303, 2002.

[47] P. Magne, "Efficient 3D finite element analysis of dental restorative procedures using micro-CT data," *Dental Materials,* vol. 23, pp. 539-548, 2007.

[48] L. A. Lang, B. Kang, R. F. Wang, and B. R. Lang, "Finite element analysis to determine implant preload," *The Journal of Prosthetic Dentistry,* vol. 90, pp. 539-546, 2003.

[49] L. Sandu, F. Topala, and N. Faur, "Three dimensional teeth designs generated by NURBS modeling," *Eur Cell Mater,* vol. 13, p. 26, 2007.

[50] L. Shi, H. Li, A. S. Fok, C. Ucer, H. Devlin, and K. Horner, "Shape optimization of dental implants," *The International Journal of Oral & Maxillofacial Implants,* vol. 22, p. 911, 2007.

[51] A. Baumgartner, L. Harzheim, and C. Mattheck, "SKO (soft kill option): the biological way to find an optimum structure topology," *International Journal of Fatigue,* vol. 14, pp. 387-393, 1992.

[52] D. Lin, Q. Li, W. Li, and M. Swain, "Dental implant induced bone remodeling and associated algorithms," *Journal of the Mechanical Behavior of Biomedical Materials,* vol. 2, pp. 410-432, 2009.

[53] N. Nathoo, M. C. Çavusoglu, M. A. Vogelbaum, and G. H. Barnett, "In touch with robotics: neurosurgery for the future," *Neurosurgery,* vol. 56, p. 421, 2005.

[54] M. Cenk Çavuşoğlu, "Medical Robotics in Surgery," *Wiley Encyclopedia of Biomedical Engineering,* 2006.

[55] L. P. Gen, A. Ejatta, F. L. Zhi, and L. X. Ping, "Review of Application of Robots in Health Care," *Pakistan Journal of Information and Technology,* vol. 1, pp. 269-271, 2002.

[56] B. L. DAVIES, "19 A Discussion of Safety Issues for Medical Robots," *Computer-Integrated Surgery: Technology and Clinical Applications,* p. 287, 1996.

[57] B. Siciliano and O. Khatib, *Springer handbook of robotics*: Springer-Verlag New York Inc, 2008.

[58] B. Siciliano, L. Sciavicco, and L. Villani, *Robotics: modelling, planning and control*: Springer Verlag, 2009.

[59] N. Van Assche, D. Van Steenberghe, M. E. Guerrero, E. Hirsch, F. Schutyser, M. Quirynen, and R. Jacobs, "Accuracy of implant placement based on pre-surgical planning of three-dimensional cone-beam images: a pilot study," *Journal of Clinical Periodontology,* vol. 34, pp. 816-821, 2007.

[60] A. Wagner, F. Wanschitz, W. Birkfellner, K. Zauza, C. Klug, K. Schicho, F. Kainberger, C. Czerny, H. Bergmann, and R. Ewers, "Computer-aided placement

of endosseous oral implants in patients after ablative tumour surgery: assessment of accuracy," *Clinical Oral Implants Research,* vol. 14, pp. 340-348, 2003.

[61] X. Sun, Y. Yoon, J. Li, and F. D. McKenzie, "An integrated computer-aided robotic system for dental implantation," *The MIDAS Journal (Systems and Architectures for Computer Assisted Interventions),* 2011.

[62] Teeth_numbers. Available:

"http://www.sundds.com/faq_tooth_teeth_numbers.htm."

VITA

Yongki Yoon was born on August 23rd, 1975 in South Korea. He received the B.S. degree in aerospace engineering from the Inha University, Incheon, South Korea, in 1999, and M.S. degrees in Mechanical and Aerospace Engineering from the Old Dominion University, Norfolk, VA, in 2008. After this, He worked at Siemens VDO Automotive from 2006 to 2008. In 2008, Yongki joined the Mechanical and Aerospace Engineering Department at Old Dominion University. He served as a teaching and research assistant during Ph.D program. He earned the Ph.D degree in Mechanical and Aerospace Engineering under the supervision of Dr. Jen-Kuang Huang in the robotics area.